Atlas of *Plasmodium falciparum* intraerythrocytic development using expansion microscopy

Benjamin Liffner[1*], Ana Karla Cepeda Diaz[2,3*], James Blauwkamp[1], David Anaguano[4,5], Sonja Frölich[6], Vasant Muralidharan[4,5], Danny W. Wilson[6,7,8], Jeffrey Dvorin[3,9], Sabrina Absalon[1#]

[1]Department of Pharmacology and Toxicology, Indiana University School of Medicine, Indianapolis, IN, USA.

[2]Biological and Biomedical Sciences, Harvard Medical School, Boston MA, USA.

[3]Division of Infectious Diseases, Boston Children's Hospital, Boston MA, USA.

[4]Center for Tropical and Emerging Global Diseases, University of Georgia, Athens, GA, USA.

[5]Department of Cellular Biology, Franklin College of Arts and Sciences, University of Georgia, Athens, GA, USA.

[6]Research Centre for Infectious Diseases, School of Biological Sciences, University of Adelaide, Adelaide, SA, Australia.

[7]Institute for Photonics and Advanced Sensing, University of Adelaide, Adelaide, SA, Australia.

[8]Burnet Institute, 85 Commercial Road, Melbourne, VIC, Australia.

[9]Department of Pediatrics, Harvard Medical School, Boston, MA, USA.

*These authors contributed equally

[#] Corresponding author

E-mail: Sabsalon@iu.edu

ABSTRACT

Apicomplexan parasites exhibit tremendous diversity in much of their fundamental cell biology, but study of these organisms using light microscopy is often hindered by their small size. Ultrastructural expansion microscopy (U-ExM) is a microscopy preparation method that physically expands the sample ~4.5x. Here, we apply U-ExM to the human malaria parasite *Plasmodium falciparum* during the asexual blood stage of its lifecycle to understand how this parasite is organized in three-dimensions. Using a combination of dye-conjugated reagents and immunostaining, we have catalogued 13 different *P. falciparum* structures or organelles across the intraerythrocytic development of this parasite and made multiple observations about fundamental parasite cell biology. We describe that the microtubule organizing center (MTOC) and its associated proteins anchor the nucleus to the parasite plasma membrane during mitosis. Furthermore, the rhoptries, Golgi, basal complex, and inner membrane complex, which form around this anchoring site while nuclei are still dividing, are concurrently segregated and maintain an association to the MTOC until the start of segmentation. We also show that the mitochondrion and apicoplast undergo sequential fission events while maintaining an MTOC association during cytokinesis. Collectively, this study represents the most detailed ultrastructural analysis of *P. falciparum* during its intraerythrocytic development to date, and sheds light on multiple poorly understood aspects of its organelle biogenesis and fundamental cell biology.

INTRODUCTION

The human malaria parasite *Plasmodium falciparum* has a complex lifecycle that involves both human and mosquito hosts. Of its many lifecycle stages, the asexual replication of *P. falciparum* inside human red blood cells (RBCs) is responsible for the clinical symptoms of malaria. This asexual blood stage starts when a merozoite invades a host RBC and transitions through several morphologies before forming approximately 30 new daughter merozoites which egress from their host cell and invade new RBCs (Figure 1a). Host RBCs are approximately 7-8 µm in diameter[1] and contain dozens of parasites, each with their own sets of organelles and structures. The small size of *P. falciparum* and its organelles still poses a challenge to the study of many facets of *P. falciparum* cell biology, especially when immunostaining is required.

Expansion microscopy, which has gained popularity over the last decade, is a set of sample preparation techniques that isotropically increase the physical size of a microscopy sample[2]. While many expansion microscopy methods have been developed, ultrastructure expansion microscopy (U-ExM)[3] was the first used in *Plasmodium* and since has been used in *P. falciparum* and across multiple apicomplexan parasites[4-9]. U-ExM results in the ~4.5 fold isotropic expansion of the sample and largely preserves its proteome, making it compatible with antibody staining and many fluorescent dyes[3]. The increase in physical sample size results in a dramatic increase in the ability to identify and distinguish different parasite structures. Thus, some structures that could previously only be investigated using electron microscopy can now be studied with the flexibility, scalability, and inexpensive nature of conventional light microscopy.

Application of U-ExM to *Plasmodium*, and other Apicomplexa, has already enhanced our understanding of parasite cell biology tremendously, resulting in the identification of new parasite structures and better characterization of the size and shape of others[4-6,10-13]. Its significant impact on the field in such a short amount of time indicates U-ExM will be a technique heavily used in both *Plasmodium* and Apicomplexa more broadly for the foreseeable future. Considering this, we set out to image *P. falciparum* structures and organelles across the asexual blood stage of the lifecycle to serve as a reference for the expanding number of U-ExM users who study Apicomplexa and to uncover previously invisible aspects of the cell biology of *P. falciparum*.

67 RESULTS

68

69 **Ultrastructure Expansion Microscopy (U-ExM) reveals multiple parasite structures without the use of**
70 **antibodies.**

71 Dyes that are not antigen-specific are commonplace in light microscopy. N-hydroxysuccinimide (NHS)
72 esters conjugated to dyes are amino-reactive and can be used for fluorescent labelling of protein density[14].
73 Similarly, BODIPY TR ceramide (BODIPY TRc) and other dye-conjugated fatty acids are commonly used
74 for labelling lipids[15]. Coupling U-ExM with these dyes has already revealed parasite structures for which
75 specific antibodies did not exist[5,6,10]. While antibody-based labelling provides high-specificity, this labelling
76 lacks complexity and is limited to the specific protein or antigen that is being targeted. The more general stains
77 increase the number of parasite features or organelles we can observe in the same sample without additional
78 antibody markers. Therefore, these general stains allow for low-specificity but high-complexity imaging,
79 similar to the use of uranyl acetate in electron microscopy[16]. To better profile the subcellular organization of
80 *P. falciparum* during the asexual blood stages, we set out to determine what parasite structures could, and
81 could not, be visualised by U-ExM when using some of these dyes.

82 We, and others, have previously shown that combining BODIPY TRc and dye-conjugated NHS ester
83 with U-ExM allows visualisation of the parasite plasma membrane (PPM), parasitophorous vacuolar
84 membrane (PVM), nuclear envelope, rhoptries, endoplasmic reticulum, microtubule organizing center
85 (MTOC), basal complex, and apical polar rings (APRs)[5,6,10]. However, many important organelles and parasite
86 structures are either not identifiable using these stains or have yet to be validated, including the mitochondrion,
87 apicoplast, and cytostomes.

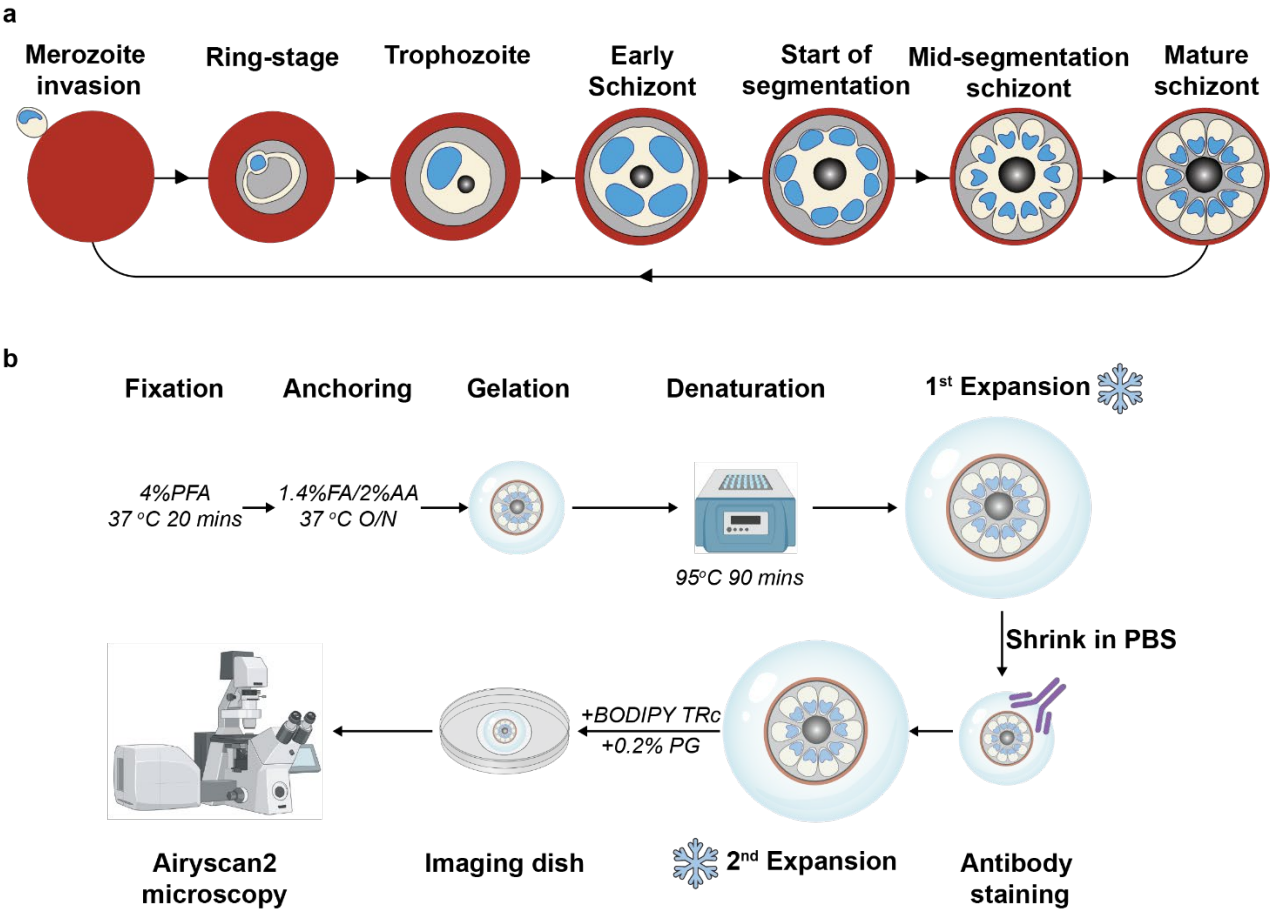

c

U-ExM *Plasmodium falciparum* (unexpanded inset)

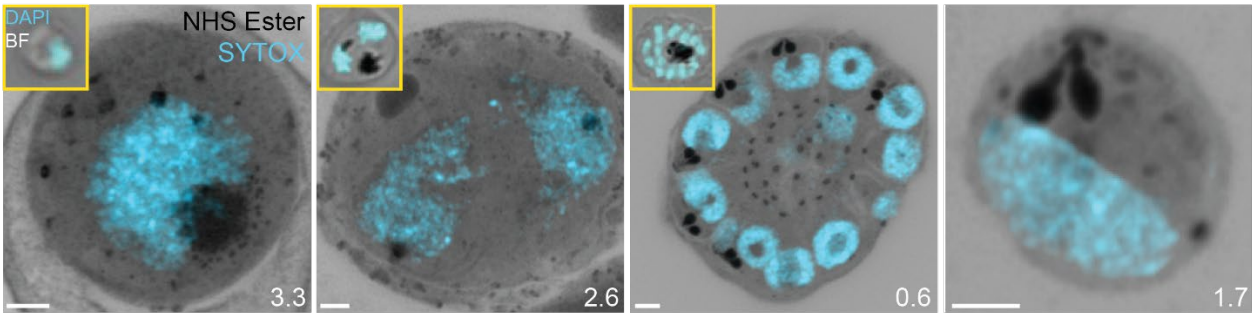

d

Organelles (and markers) imaged in this study			
MTOC (Centrin)	Microtubules (Tubulin)	Basal Complex (CINCH)	Mitochondrion (ATPd/MitoTracker)
Apicoplast ($ACP^{TS\text{-}GFP}$)	Cytostomes ($K13^{GFP}$)	Rhoptry neck (RON4)	Rhoptry bulb (RAP1/RAMA)
Micronemes (AMA1/EBA175)	Cytoplasm (Aldolase)	Endoplasmic reticulum (BIP)	Golgi (ERD2)
Inner membrane complex (GAP45/IMC1g)			

Figure 1: U-ExM workflow and summary of parasite structures imaged in this study.

(a) *Asexual blood stage lifecycle of P. falciparum.* ***(b)*** *Ultrastructure expansion microscopy (U-ExM) workflow used in this study. PFA = paraformaldehyde, FA = formaldehyde, AA = acrylamide PG = propyl gallate. Snowflake indicates steps where gels were cryopreserved.* ***(c)*** *Comparison of brightfield and DAPI staining of unexpanded P. falciparum parasites (inset) with P. falciparum prepared by U-ExM, stained with NHS Ester (protein density; greyscale) and SYTOX Deep Red (DNA; cyan) and imaged using Airyscan microscopy. Images are maximum-intensity projections, number on image = Z-axis thickness of projection in µm. Scale bars = 2 µm.* ***(d)*** *Summary of all organelles, and their corresponding antibodies, imaged by U-ExM in this study.*

96 To identify and validate the location of as many parasite organelles and structures as possible, we
97 utilized U-ExM coupled with BODIPY TRc, Alexa Fluor 405-conjugated NHS ester (which we will refer to
98 as "NHS ester"), the nucleic acid (i.e., DNA) stain SYTOX Deep Red, and antibodies directed against 13
99 different subcellular targets (microtubules, MTOC, basal complex, IMC, mitochondrion, apicoplast,
100 cytostome, rhoptry bulb, rhoptry neck, micronemes, cytoplasm, endoplasmic reticulum, and Golgi). Parasites
101 were harvested at multiple time points during the intraerythrocytic asexual stage and imaged using Airyscan2
102 super-resolution microscopy, providing high-resolution three-dimensional imaging data (Figure 1c). A full
103 summary of all target-specific stains used in this study can be found in Figure 1d.

104 The first protein we imaged was aldolase, a marker of the parasite cytoplasm (Supplementary Figure
105 1). Aldolase staining was present in all asexual replication stages. During the ring stage, the "ameboid" shape
106 of the parasite is readily visualized, consistent with previous studies of this stage in time-lapse microscopy of
107 live parasites[17] (Supplementary Figure 1). Regions within the parasite where both aldolase and NHS ester
108 staining were absent are consistent with the expected area of the food vacuole. Typically, the food vacuole
109 would be filled with hemozoin, however, this crystal likely cannot expand and therefore leaves a large space
110 inside the parasite that does not contain significant protein density (Supplementary Figure 1).

111

112 **The microtubule organizing center (MTOC) and microtubules.**

113 The first major transition during the blood stage of the lifecycle occurs when the parasites turn from
114 rings into trophozoites. Soon after this transition, the parasite will begin to replicate its DNA and undergo
115 mitosis followed by nuclear fission[18]. Mitosis is coordinated by microtubules, which are in turn nucleated by
116 structures called microtubule organizing centers (MTOCs)[19]. It was recently shown that the nuclear MTOC
117 which coordinates *P. falciparum* mitosis is comprised of intranuclear and cytoplasmic portions[10]. The most
118 commonly used MTOC markers are the centrins, which in *Plasmodium* comprise four proteins that localize
119 to the cytoplasmic portion of the MTOC and appear after intranuclear microtubules have already formed [10].
120 Given that the MTOC is required for microtubule formation, this implies that the MTOC forms before centrin
121 is visible. To investigate these processes in more detail, we visualized the biogenesis and dynamics of the

122 MTOC and microtubules during the trophozoite and schizont stages by pairing NHS ester, which we have
123 recently shown can stain both the intranuclear and cytoplasmic portions of the MTOC[6], with an anti-centrin
124 antibody (Clone 20H5, raised against centrin from *Chlamydomonas*). This antibody likely recognizes centrin
125 3 in *P. falciparum*[20], but a recent study suggests that all four *P. falciparum* centrins share an MTOC
126 localization[21].

127 *MTOC biogenesis and disassembly*

128 Neither a recognizable MTOC nor above-background centrin staining were observed in ring-stage
129 parasites (Figure 2b)[10]. The MTOC first appeared in mononucleated trophozoites but changed morphology as
130 these parasites got closer to their first nuclear division. In the 23 mononucleated trophozoites we imaged, 52%
131 of MTOCs lacked cytoplasmic extensions (Supplementary Figure 2a&b). These MTOCs only had their
132 intranuclear portion, lacking cytoplasmic extensions as observed by NHS ester (Figure 2a&b). We will refer
133 to this as the 'early' MTOC. All 12 of the 'early' MTOC trophozoites we imaged also lacked centrin staining
134 (Supplementary Figure 2c). This matches previous reports that centrin is specifically associated with the
135 cytoplasmic domain of the MTOC[10]. As expected, this 'early' MTOC was capable of nucleating microtubules
136 (Supplementary Figure 2a). The centrin focus and cytoplasmic extensions became visible in mononucleated
137 trophozoites after nucleation of the intranuclear microtubules but prior to the first MTOC duplication event
138 (Supplementary Figure 2a), consistent with previous reports[10]. The cytoplasmic extensions of the MTOC
139 began at the nuclear membrane and ended at an NHS ester-dense focus located at the parasite plasma
140 membrane (PPM) (Figure 2b). This association between the nuclear MTOC and the PPM has previously been
141 observed in gametocytes and asexual blood stages[22,23], but the temporal nature of this association during the
142 asexual blood stages remained uncharacterized. Our observation of cytoplasmic tethers by NHS ester,
143 discussed further below, combined with the temporal pattern of MTOC-PPM association suggests that nuclei
144 are physically anchored to the PPM while parasites are undergoing mitosis.

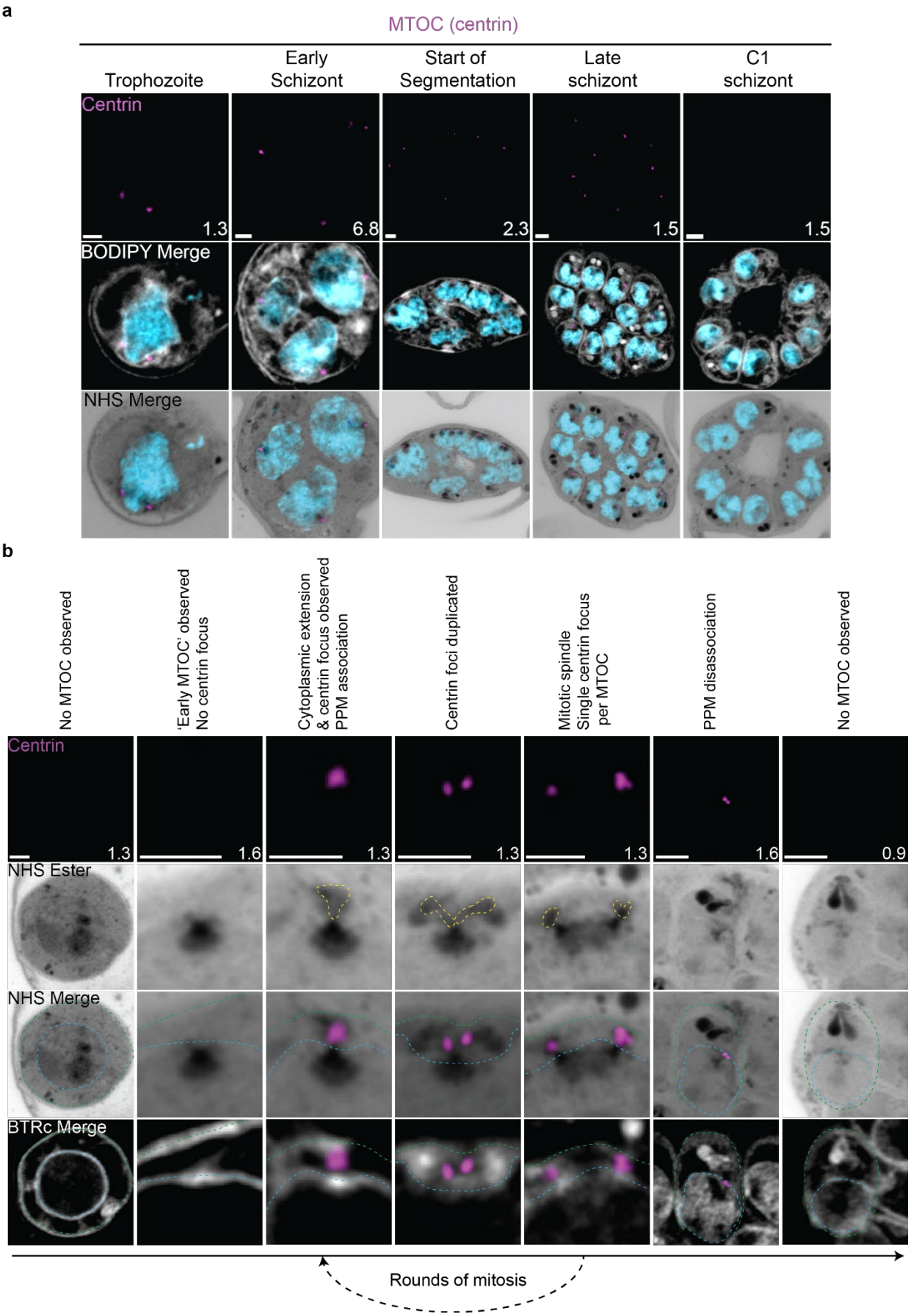

Figure 2: Microtubule organizing center (MTOC) biogenesis and dynamics.
(a) *3D7 parasites were prepared by U-ExM, stained with NHS ester (greyscale), BODIPY TRc (white), SYTOX (cyan) and anti-centrin (MTOC; magenta) antibodies and imaged using Airyscan microscopy across the asexual blood stage.* ***(b)*** *Proposed timeline of events in MTOC biogenesis, dynamics, and disassembly. Yellow line = cytoplasmic extensions, blue line = nuclear envelope, green line = parasite plasma membrane. Images are maximum-intensity projections, number on image = Z-axis thickness of projection in µm. Scale bars = 2 µm.*

152 For as long as parasites continue to undergo mitosis throughout schizogony, all MTOC cytoplasmic
153 extensions remain in contact with the PPM (Figure 2a). These cytoplasmic extensions showed one or two
154 centrin foci that largely matched branch number. That is, of the 102 single-branched MTOCs observed, all
155 had a single centrin focus, and of the 28 double-branched MTOCs observed, 92% had two centrin foci (Figure
156 2b; Supplementary Figure 2c). The overwhelming coordination between number of cytoplasmic extensions
157 and number of centrin foci suggests centrin duplication and duplication of the cytoplasmic tethers of the
158 MTOC happens quickly and simultaneously. The few cases when there is a mismatch between the number of
159 cytoplasmic extensions and centrin foci all occur in double-branched MTOCs and can be attributed to
160 limitations in our ability to resolve two centrin foci (Supplementary Figure 2c&d).

161 The relative abundance of nuclei with single MTOCS, defined as MTOCs lacking a mitotic spindle,
162 versus mitotic MTOCs, MTOCs anchored to a mitotic spindle, varied throughout schizogony as did their
163 branch numbers (Supplementary Figure 2). We hypothesize that MTOCs start out without any cytoplasmic
164 extensions and then develop a single cytoplasmic extension and centrin focus which duplicate ahead of MTOC
165 duplication and then segregate with each MTOC during miotic spindle formation and karyokinesis (Figure
166 2b). This means that during the rapid mitotic events of schizogony that take place at the 6-12 nuclei stage,
167 single MTOCs with a single cytoplasmic extension are very rare. We observed them in just 6% of 221 imaged
168 MTOCs (Supplementary Figure 2b). Single MTOCs with a single cytoplasmic extension were only abundant
169 when the pace of nuclear replication was slow at the early schizont stage (24% of 76 MTOCs imaged in cells
170 with 2-5nuclei) and the end of segmentation (44% of 290 MTOCs imaged in segmenting parasites).

171 This observed pattern of duplication and segregation also suggests that double-branched MTOCs with
172 two centrin foci have committed to undergoing a new round of mitosis and that the duplication of cytoplasmic
173 extensions represents the first identifiable step in MTOC duplication. In line with this hypothesis, the most
174 common MTOC states in schizonts prior to segmentation are single MTOCs with 2 cytoplasmic extensions
175 (26% of MTOCs in cells with 2-5 nuclei, 52% in cells with 6-12 nuclei) which have committed to the next
176 round of mitosis and mitotic MTOCs with one extension each (42% of MTOCs in cells with 2-5 nuclei, 36%
177 in cells with 6-12 nuclei) which are finishing a round of mitosis. Interestingly, 8% of MTOCs observed in the
178 2-5 nuclei stage and 6% in the 6-12 nuclei stage were mitotic and double-branched, suggesting the duplication

179 of cytoplasmic extensions, and commitment to the next round of mitosis, can happen before karyokinesis is
180 completed (Supplementary Figure 2b & 3).

181 MTOCs reach semi-synchrony at the beginning of segmentation as defined by the first appearance of
182 a basal complex by NHS ester. At this point, rather than seeing a variety of MTOC states and branch numbers,
183 virtually all MTOCs in the same cell share the same mitotic state and branch number. Most MTOCs appear
184 as mitotic MTOCs with a single cytoplasmic extension during early segmentation and then appear as single
185 MTOCs with a single extension during mid-segmentation (Supplementary Figure 2b). By the time
186 segmentation is completed, the MTOC is no longer visible by NHS ester, suggesting that the nuclear MTOC
187 may disassemble after all mitotic events are finished (Supplementary Figure 2b and Figure 2b). Of 159 nuclei
188 imaged in 6 C1-arrested schizonts, none showed the presence of an MTOC.

189 *The apical polar rings, Golgi, and rhoptries are all segregated with the MTOC.*

190 Given the cytoplasmic coordination of mitotic events and the physical tethering of the nucleus to the
191 PPM throughout schizogony, we investigated whether we could observe any coordination extending to the
192 apical organelles and other structures known to be present near the MTOC at these stages. We observed close
193 association between the cytoplasmic extensions of the MTOC and the rhoptries, Golgi, basal complex, and
194 APR.

195 The number of basal complex structures closely matched the number of MTOC cytoplasmic extensions
196 throughout schizogony. No basal complex structures were observed in MTOCs without cytoplasmic
197 extensions. Of 82 single-branched MTOCs imaged, 81 (99%) showed a single basal complex structure. Of 37
198 double-branched MTOCs imaged, 33 (89%) showed two basal complex structures. As we observed when
199 imaging centrin foci, the few cases when there is a mismatch between the number of cytoplasmic extensions
200 and basal complex structures mostly occur in double-branched MTOCs. However, in this case, the mismatch
201 cannot be attributed to resolution as CINCH staining of the basal complex remains punctate until early
202 segmentation (Figure 4b). Thus, this mismatch between number of cytoplasmic extensions and basal complex
203 structures most likely reflect a transition state. This suggests that basal complex division, when visualized by
204 breaks in CINCH staining, is less simultaneous with MTOC branch duplication than centrin focus duplication.

205 Rhoptry biogenesis, discussed further below, was also closely tied to the number and position of the
206 MTOC cytoplasmic extensions. This association of one rhoptry per branch, however, is broken at the start of
207 segmentation, when 205 of 211 imaged MTOCs (97%) had a rhoptry pair per MTOC branch. Further
208 suggestive of MTOC-rhoptry interaction is the fact that the rhoptries were positioned immediately next to the
209 MTOC cytoplasmic extensions for as long as these were visible by NHS ester. While we had no APR protein
210 marker, the cytoplasmic extensions always ended in an NHS ester-dense focus at the plasma membrane. At
211 the beginning of segmentation, this focus obtained a morphology suggestive of the APR based on its ring
212 shape, position, and size. As described above, a small percentage of parasites commit to the next round of
213 mitosis before they finish segregating their genetic material. In these parasites, MTOC-associated organelles
214 continued to match the number of cytoplasmic extensions. This gave rise to nuclei that were anchored to four
215 basal complexes, four single rhoptries, and four APR densities in close proximity (Supplementary Figure 3).
216 This matches previous observations by three-dimensional electron microscopy that a single nucleus can have
217 4 sets of apical buds[16].

218 We also characterized the distribution of the Golgi and its association with the MTOC. The Golgi was
219 visualised using an antibody to ER lumen protein retaining receptor 2 (ERD2), a cis-Golgi marker expressed
220 throughout intraerythrocytic development[24] (Supplementary Figure 4). Small regions of Golgi were visible at
221 all development stages. In ring-stage parasites and mononucleated trophozoites, one or two Golgi foci were
222 observed near the nucleus but had no MTOC association. In all 5 imaged parasites with less than 2 nuclei and
223 lacking MTOC cytoplasmic extensions, no Golgi was observed near the MTOC. In parasites that had
224 undergone the first round of mitosis and had developed MTOC cytoplasmic extensions, the Golgi was
225 proximal to these extensions (Supplementary Figure 2b and Supplementary Figure 4) and closely matched
226 their number and presence. Specifically, 21 of 22 imaged parasites with visible cytoplasmic extensions had
227 Golgi staining associated with each of their MTOCs (Supplementary Figure 2b). While Golgi-MTOC
228 association coincides with the appearance of the cytoplasmic extensions, the Golgi is able to remain at the
229 apical end of the parasite after these tethers and the MTOC are no longer visible by NHS ester. In C1-arrested
230 schizonts, each merozoite has a single Golgi that remains at the apical end of the parasite, typically between
231 the rhoptry bulb and the nucleus (Supplementary Figure 4).

232 In contrast, we did not observe an MTOC association in the distribution of the endoplasmic reticulum
233 (ER) (Supplementary Figure 5) within the parasite. The ER was visualised using an antibody to Binding
234 Immunoglobulin Protein (BIP), a constitutively expressed ER lumen protein[25]. As expected, ER was detected
235 at all stages of intraerythrocytic development (Supplementary Figure 5). In ring-stage and mononucleated
236 trophozoite-stage parasites, the ER could be seen wrapping around the nucleus and forming recognizable
237 cisternae. In multinucleated parasites, the ER was too dense to observe cisternae, but large regions of the cell
238 were occupied by the ER. Following segmentation in C1-arrested schizonts, the ER was only observed
239 contiguous with the nuclear envelope.

240 Combining the observations that the MTOC is physically tethered to the PPM by its cytoplasmic
241 extensions and that this anchoring is closely associated with organelles that will define the apical end of the
242 parasite (nuclear pore complexes[10], Golgi, rhoptries, basal complex, and apical polar rings), we suggest that
243 this tethering by the MTOC cytoplasmic extensions establishes apical-basal polarity in the parasite early in
244 schizogony. Considering that rhoptries are formed from Golgi-derived cargo[26,27], it is unsurprising to find the
245 Golgi forms part of this apical cluster of organelles throughout schizogony. The confined space between
246 nuclear envelope and PPM that these organelles are packed into, for example, may provide a mechanism for
247 each nucleus to provide rhoptry cargo locally to their own rhoptries rather than to all rhoptries in the cell. The
248 same principle could apply to other apical Golgi-derived organelles. However, it remains unclear what role
249 the MTOC cytoplasmic tethers play in this association, whether any organelles besides the nucleus are
250 physically tethered by these extensions, and how these clusters of organelles remain together during the rapid
251 mitotic events constantly separating sister MTOCs.

252 *Characterisation of intranuclear microtubules.*

253 *P. falciparum* is known to have two classes of microtubules; intranuclear microtubules that partake in
254 mitosis[6,10], and subpellicular microtubules (SPMTs) that are cytosolic and extend in a single spine from the
255 apical end of merozoites[6,10]. Investigating microtubules with an anti-α-tubulin antibody, we failed to detect
256 microtubules in ring-stage parasites, consistent with previous observations (Supplementary Figure 6)[10].
257 Intranuclear microtubules were first visible in mononucleated trophozoite-stage parasites and were present
258 until early segmentation stages, with no intranuclear microtubules visible by the end of segmentation (Figure

3a). Intranuclear microtubules arrange into three distinct spindle structures: hemispindles, mitotic spindles, and interpolar spindles. Hemispindles are microtubule structures coming from a single MTOC that retract prior to MTOC duplication. Mitotic spindles appear following MTOC duplication and separate sister chromatids during mitosis. When the two MTOCs migrate away from each other, they remain connected by an elongated microtubule structure called the interpolar spindle (or elongated spindle), which retracts prior to nuclear fission[10,28,29]. It has recently been shown that the interpolar spindle is short-lived relative to the hemispindle and mitotic spindle[10,28]. In this study, we observed 24 interpolar spindles, which allowed us to perform the first detailed characterisation of this spindle type (Figure 3b).

Interpolar spindles have microtubule branches that connect the two distant MTOCs (interpolar microtubules), and microtubule branches that do not connect the MTOCs (non-interpolar microtubules). Each interpolar spindle contained an average of 12.5 (± 2.6 SD) total microtubules, of which 1.3 (± 0.6 SD) were interpolar microtubules and 11.2 (± 2.8 SD) were non-interpolar microtubules (Figure 3c). The average number of non-interpolar branches per MTOC was 5.6, which is similar to the previously reported average number of branches in a hemispindle of 5 to 6[6,10]. This suggests that only the interpolar microtubules retract during the interpolar spindle to hemispindle transition. We measured interpolar microtubules in 3D, adjusting for expansion factor by dividing the measured distance by 4.25, the median expansion factor observed in this study (Supplementary Figure 7a&b; Materials and Methods). Interpolar microtubules ranged from ~1-5 µm, with a mean length of 2.9 µm (± 1.0 µm SD) or 12.47 µm before expansion factor correction (Figure 3d). In all cases, the MTOCs connected by interpolar spindles were anchored to the plasma membrane by their cytoplasmic extensions. The large variability in interpolar microtubule size and the continued tethering of the MTOCs to the PPM suggest that interpolar microtubules push PPM-anchored MTOCs to opposite sides of the cell without causing detachment from the PPM. It is unclear how parasites achieve this sliding effect or how MTOC-associated organelles are able to retain this association while MTOCs are moved large distances.

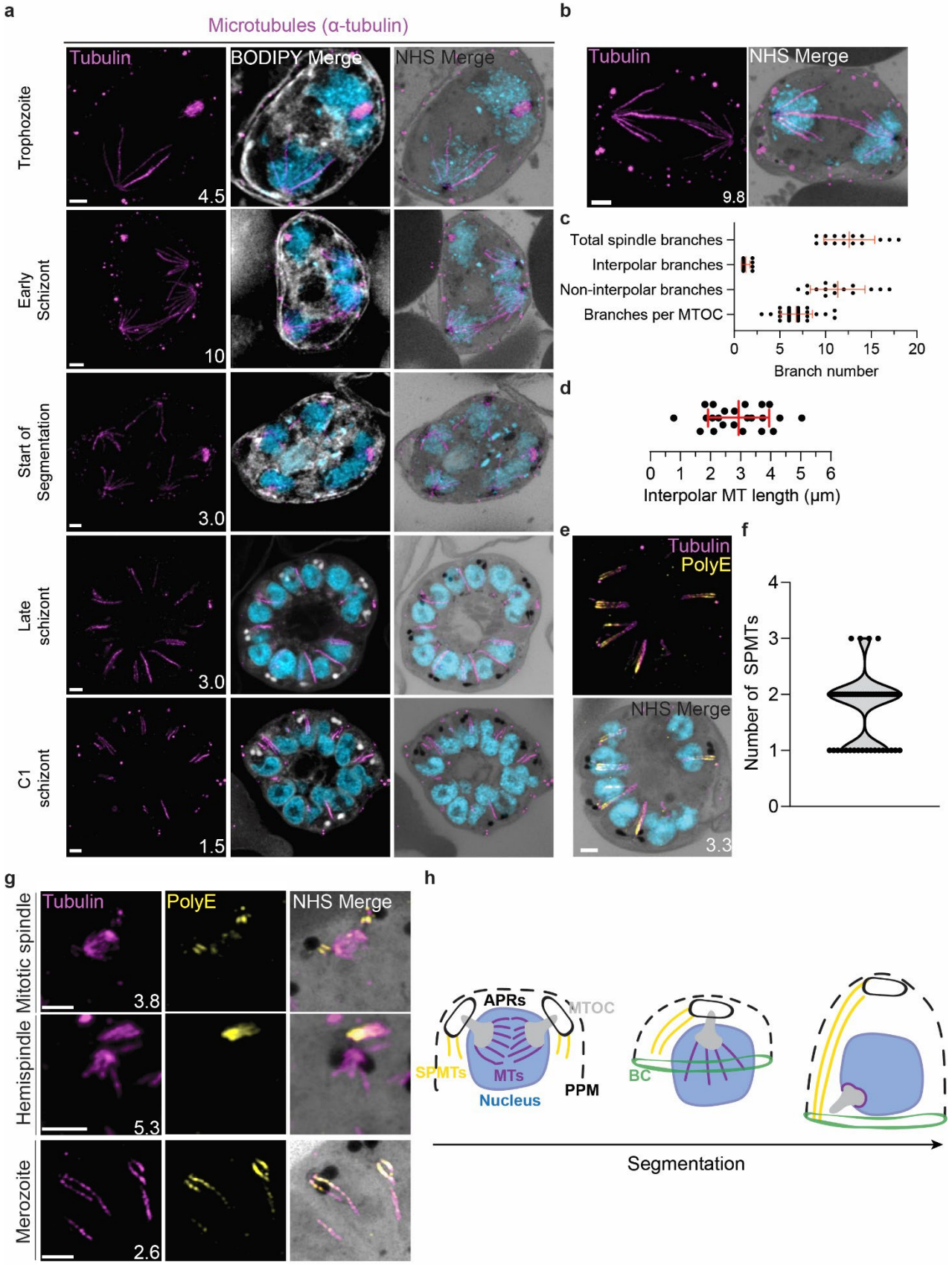

Figure 3: Characterisation of intranuclear and subpellicular microtubules.
(a) *3D7 parasites were prepared by U-ExM, stained with NHS ester (greyscale), BODIPY TRc (white), SYTOX (cyan) and anti-tubulin (microtubules; magenta) antibodies, and imaged using Airyscan microscopy across the asexual blood stage.* ***(b)*** *Nuclei in the process of dividing, with their MTOCs connected by an interpolar spindle.* ***(c)*** *The number and type of microtubule branches in interpolar spindles and* ***(d)*** *length of interpolar microtubules.* ***(e)*** *Subpellicular microtubules (SPMTs) stained with an anti-poly-glutamylation (PolyE; yellow) antibody.* ***(f)*** *Quantification of the number of SPMTs per merozoite from C1-treated schizonts.* ***(g)*** *SPMT biogenesis throughout segmentation.* ***(h)*** *Model for SPMT biogenesis. PPM = parasite plasma membrane, APRs = apical polar rings, BC = basal complex. Images are maximum-intensity projections, number on image = Z-axis thickness of projection in µm. Scale bars = 2 µm.*

293 *Subpellicular microtubule length and biogenesis.*

294 Subpellicular microtubules are nucleated in the cytoplasm and have long been observed in merozoites[30].
295 SPMTs have been shown to be stabilised by polyglutamylation[5] and can be identified specifically using a
296 combination of anti-tubulin and anti-PolyE antibodies (Figure 3e). Using this approach, we characterised 86
297 SPMTs in 50 merozoites from C1-arrested schizonts. These nascent merozoites had between 1 and 3 SPMTs,
298 with an average of 1.7 (± 0.6 SD) (Figure 3f). Of 50 imaged merozoites, 48 had at least one SPMT that
299 extended >50% of cell length from the apical polar ring to the basal complex. This longest microtubule in a
300 merozoite had an average length of 1.01 µm (± 0.24 µm SD). In merozoites with more than one SPMT, the
301 second and third microtubules were shorter than the first, having an average length of 0.8 µm (± 0.21 µm SD).
302 Given the large variation in SPMT size and observation that, in segmenting schizonts, the basal end of the
303 SPMTs was in contact with the basal complex throughout segmentation, we hypothesise that most SPMTs
304 measured in our C1-treated schizonts had partially depolymerised. *P. falciparum* microtubules are known to
305 rapidly depolymerise during fixation[10,29]. It is unclear, however, why this depolymerization was observed most
306 often in C1-arrested parasites. Thus, we cannot determine whether these shorter microtubules are a by-product
307 of drug-induced arrest or a biologically relevant native state that occurs at the end of segmentation.

308 Little is known about SPMT biogenesis during the asexual blood stage of *P. falciparum*, but it is
309 currently hypothesized that they are nucleated by the apical polar rings[31,32], as is the case in *Toxoplasma*[32,33].
310 Curiously, TgCentrin 2 localizes to the apical polar ring of *Toxoplasma* tachyzoites[34], but no Centrin 2 has
311 been observed to localize to the apical polar rings of *P. falciparum*. Furthermore, it was recently shown that
312 the SPMTs of *P. falciparum* gametocytes, which lack an APR, are formed at the cytoplasmic extensions of
313 the nuclear MTOC, in the space between the nuclear envelope and PPM[22]. Leveraging our ability to
314 specifically detect SPMTs using PolyE, we investigated the possibility that merozoite SPMTs are also formed
315 at the cytoplasmic extensions and subsequently transferred onto the apical polar ring during segmentation. In
316 schizonts where nuclei are approaching or have completed their final mitosis (~15n), we observed small
317 cytoplasmic microtubules that stained strongly with PolyE appear in the area between the nuclear MTOC and
318 PPM (Figure 3g). However, we did not achieve a resolution that allowed us to distinguish individual APRs or

319 to confidently pinpoint whether the microtubules were nucleated at the APRs or the cytoplasmic extensions.
320 Likely, higher resolution imaging techniques are needed to resolve the site of SPMT nucleation in merozoites.
321

322 **Segmentation machinery (inner membrane complex and basal complex)**

323 Following replication of their genetic material during the trophozoite and early schizont stages,
324 parasites partition their nuclei and organelles into ~30 daughter merozoites from the common cytoplasm of a
325 schizont[35]. This form of cytokinesis, called segmentation, takes place in the final hours of schizogony and
326 culminates with the physical separation of each daughter cell and their egress from the host RBC. The inner
327 membrane complex (IMC) is a double lipid bilayer formed from flattened vesicles that scaffolds the process
328 of segmentation as well as anchors many proteins important for parasite shape and motility[36].

329 *The IMC cannot be distinguished from the plasma membrane by U-ExM*

330 The IMC forms *de novo* during segmentation starting at the apical end of the parasite, where the MTOC
331 is anchored to the plasma membrane (Supplementary Figure 8a)[36]. This can be observed using the IMC-
332 anchored protein Glideosome associated protein 45 (GAP45), which bridges the IMC and plasma membrane,
333 as well as using BODIPY TRc, which shows increased membrane staining in the area overlapping GAP45[37]
334 (Supplementary figure 8a). As segmentation progresses, the IMC expands around the nucleus and associated
335 organelles until it envelops the daughter cell, leaving an opening at the apical end, where the apical polar ring
336 is located, and the basal end, where the basal complex resides (Supplementary Figure 8a). While the pellicle
337 was easily visualized as a whole, we were unable to distinguish the IMC membranes from the PPM
338 (Supplementary Figure 8b&c). We stained parasites using the plasma membrane marker MSP1 and two
339 different IMC markers: GAP45, which lies between the IMC and PPM, and IMC1g, which is attached to the
340 cytoplasmic face of the IMC[38,39]. In both cases we were unable to resolve the IMC marker from MSP1
341 (Supplementary Figure 8b&c).

342 *Basal complex dynamics throughout segmentation*

343 The basal complex is an essential ring structure located at the basal end of the IMC[40]. It is hypothesized
344 to act as a contractile ring that guides IMC biogenesis and mediates abscission of newly formed merozoites
345 by separating the IMC and plasma membrane from the residual body. We used parasites where PfCINCH, a

346 basal complex marker, was tagged with an smV5 tag to follow basal complex development throughout
347 schizogony (Figure 4)[41]. CINCH is first visible at early schizogony (3-5 nuclei stage) as a small ring-like
348 structure surrounding an NHS ester-dense focus on the plasma membrane that is tethered to the MTOC (Figure
349 4). Of 55 early schizont MTOCs imaged, 44 (80%) had matching numbers of MTOC cytoplasmic extensions
350 and basal complex structures. This suggests that as MTOCs divide, they each inherit a CINCH ring that has
351 been split by the duplication of the cytoplasmic tethers (Figure 4b). During the rapid nuclear divisions of
352 schizogony, 77% of the CINCH structures of mitotic MTOCs show a break in the ring. This break faces a
353 sister basal complex with its own cytoplasmic extension (Figure 4b and Supplementary Figure 3). So, when
354 we see duplication of the MTOC's cytoplasmic extensions, the basal complex ring "breaks" into two
355 semicircles which re-seal to form their own ring prior to the next branch duplication (Figure 4b).

356 Once segmentation begins and the MTOC's cytoplasmic extensions stop duplicating, CINCH forms a
357 *bona fide* ring with smooth borders (Figure 4). At this point, nuclei reach a point of semi-synchronicity. All
358 64 imaged MTOCs in early segmentation parasites had duplicated MTOCs forming a mitotic spindle and each
359 MTOC had a single uninterrupted basal complex ring (Figure 4b). This event marks the last nuclear division
360 the parasite will undergo. Thus, we cease to observe events where a single nucleus is attached to four basal
361 complexes as MTOCs have ceased committing to future rounds of mitosis. By the time the basal complex
362 reaches its maximum diameter, all nuclear divisions have been completed, each nucleus has a single MTOC
363 and basal complex, and no mitotic spindles are visible (Figure 4). After this point, the basal complex contracts
364 and moves in the basal direction away from the apical end. By the time segmentation is completed, the basal
365 complex is an NHS ester dense ring that is smaller than the apical polar ring.

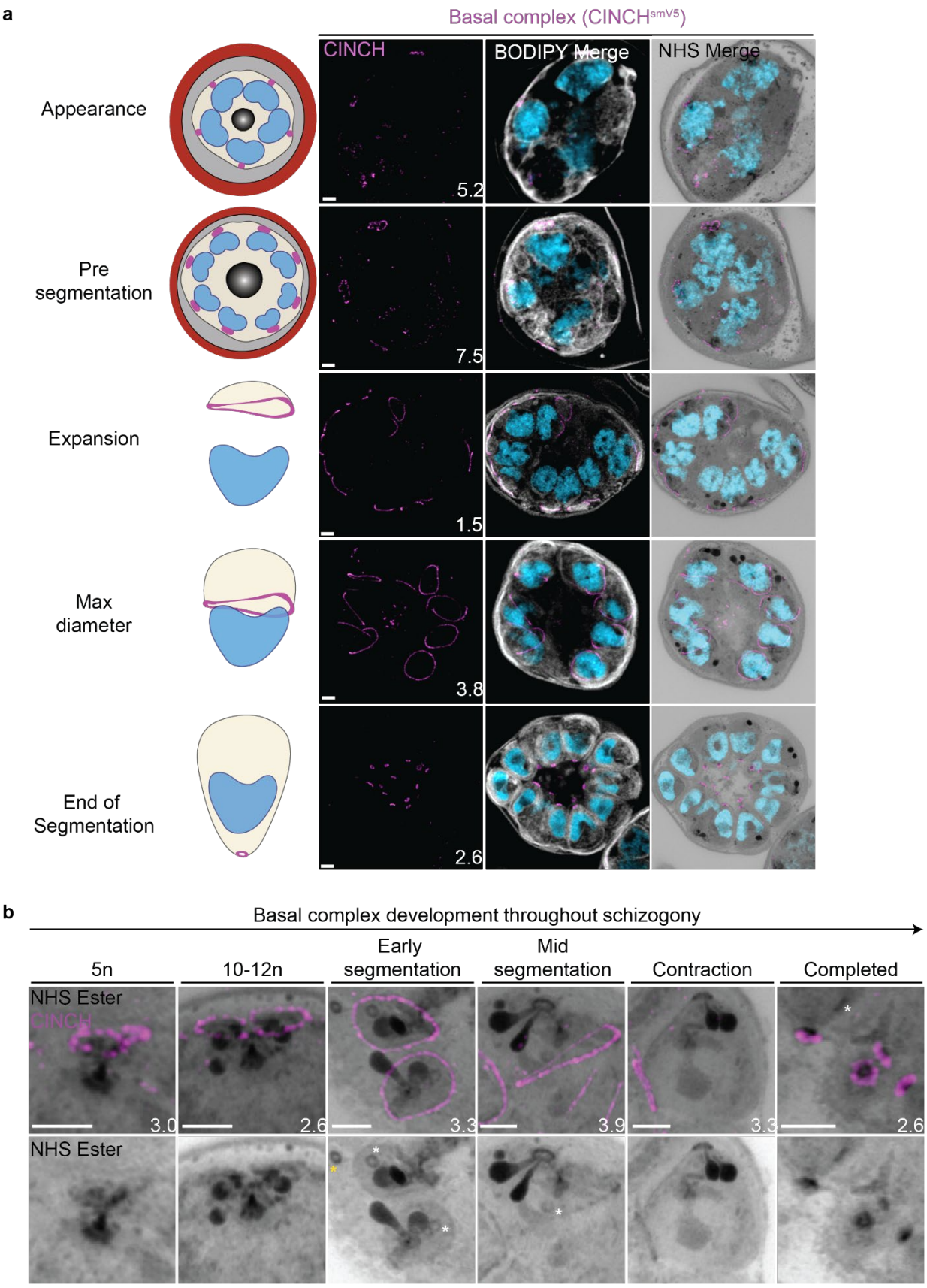

Figure 4: Basal complex biogenesis and development throughout segmentation.
(a) *Parasites expressing an smV5-tagged copy of the basal complex marker CINCH were prepared by U-ExM, stained with NHS ester (greyscale), BODIPY TRc (white), SYTOX (cyan) and anti-V5 (basal complex; magenta) antibodies and imaged using Airyscan microscopy across segmentation.* ***(b)*** *Basal complex development during schizogony. The basal complex is formed around the PPM anchor of the MTOC. In nuclei whose MTOC has two cytoplasmic extensions, and will therefore undergo mitosis, the basal complex rings are duplicated. From early segmentation, the basal complex acquires a stable, expanding ring form. Cytostomes that will form part of merozoites are marked with a white asterisk, while those outside merozoites are marked with a yellow asterisk. Images are maximum-intensity projections, number on image = Z-axis thickness of projection in µm. Scale bars = 2 µm.*

375 *NHS ester as a basal complex marker*

376 While the basal complex stains brightly with NHS ester at the end of segmentation (Figure 4), this
377 staining is not consistent throughout schizogony. Since NHS ester is an indicator of protein density, changes
378 in basal complex staining could indicate a relative change in protein abundance at the basal complex. NHS-
379 ester staining of the basal complex is not visible or is very faint during early schizogony. Once the basal
380 complex attains its *bona fide* ring form during early segmentation, it stains reliably, though faintly, with NHS
381 ester. This staining intensifies after the basal complex begins to contract. This denser staining could be due to
382 recruitment of more basal complex proteins at the midpoint of schizogony, an increase in protein density as
383 the ring area decreases during contraction, or both. Once the parasites finish segmentation, the basal complex
384 is at its brightest (Figure 4b). While NHS ester staining correlates with CINCH, it does not perfectly overlap
385 with it. CINCH consistently appears as a larger ring with a slight basal shift relative to NHS ester after the
386 basal complex reaches maximum diameter, an effect most visible at the end of segmentation (Figure 4b). Since
387 this shift is consistent with parasite anatomy regardless of parasite orientation, it suggests it is not an imaging
388 artifact. There is no primary antibody against CINCH at this point, and so it is not possible to determine
389 whether the lack of overlap with NHS ester is due to distance between the smV5 tag and the main protein
390 density of CINCH (CINCH is 230kDa). It is also possible that this difference in localization reflects basal
391 complex architecture similar to that previously observed in *Toxoplasma gondii*, where the basal complex
392 consists of multiple concentric rings[34,42,43 44].

393

394 **Mitochondrion and apicoplast**

395 The apicoplast and mitochondrion undergo pronounced morphological changes during the *P.*
396 *falciparum* blood-stage lifecycle [45,46]. Both are long, and often branching, organelles whose complex three-
397 dimensional morphologies have only been robustly studied using electron microscopy-based techniques[16].

398 *Looped regions of the mitochondrion display low membrane potential.*

399 To visualize the mitochondria, we stained live parasites using Mitotracker Orange CMTMRos prior to
400 fixation and expansion (Supplementary Figure 9a). Mitotracker Orange CMTMRos accumulates in live
401 mitochondria, driven electrophoretically by membrane potential, and is retained after fixation[47,48]. When

402 imaged at high resolution, Mitotracker can be used to observe individual cristae in the mitochondria of
403 mammalian cells[49]. *Plasmodium* cristae morphology is different from that found in mammalian mitochondria;
404 cristae are thought to be bulbous or tubular rather than lamellar and are present in gametocytes but absent
405 from asexual blood-stage parasites[50,51]. To our surprise, rather than showing continuous staining of the
406 mitochondria, Mitotracker staining of our expanded parasites revealed alternating regions of bright and dim
407 staining that formed Mitotracker-enriched pockets (Supplementary Figure 9b). These clustered areas of
408 Mitotracker staining were highly heterogeneous in size and pattern and seemed to indicate that regions of high
409 membrane potential are confined to specific regions of the organelle. Small staining discontinuities like these
410 are commonly observed in mammalian cells when using Mitotracker dyes due to the heterogeneity of
411 membrane potential from cristae to cristae as well as due to fixation artifacts. While our observed Mitotracker-
412 enriched pockets could be a fixation artifact or be a product of local membrane depolarization, we cannot
413 discard the possibility that regions of brighter staining represent Mitotracker accumulation inside irregular
414 compartments of high membrane potential within the mitochondrion.

415 In addition to these small staining discontinuities, we observed large gaps in Mitotracker staining
416 within parasites at all stages of development. This included pre-segmentation parasites, where we would
417 expect a single continuous mitochondrion to be present (Supplementary Figure 9a). To our knowledge, no
418 membrane potential discontinuities or fixation artifacts of this size have been reported in mammalian cells.
419 So, as a secondary way to visualise the mitochondria and better characterize these staining discontinuities, we
420 generated a transgenic cell line with the putative ATP synthase F0 subunit-d (ATPd, Pf3D7_0311800) tagged
421 with a spaghetti monster HA tag[52] (Supplementary Figure 10). ATPd is a membrane-embedded proton channel
422 that had not previously been localized to the mitochondria in *P. falciparum* but was identified as a
423 mitochondrial protein in a recent proteomics study[51,53]. Furthermore, its *Toxoplasma* homologue has been
424 shown to localize to the mitochondria[54,55]. We confirmed that ATP synthase subunit F0 localizes to *P.*
425 *falciparum* mitochondria, as it largely co-localized with Mitotracker staining, forming a border around it due
426 to its membrane association (Supplementary Figure 9a). ATPd, like Mitotracker, had a heterogenous
427 distribution throughout the mitochondria, but it did not show the same large gaps in staining. ATPd allowed
428 us to better visualize regions of the mitochondria that appeared to fold onto themselves and fuse with each

429 other, as has been previously described[45]. Thus, Mitotracker and ATPd are both useful but imperfect markers
430 for the mitochondria, with neither of them showing a continuous, even distribution throughout the organelle.

431 Curiously, 25 of 26 imaged parasites showed Mitotracker discontinuities specifically in regions where
432 the ATPd signal formed looped structures (Figure 5b). These structures were defined as areas where the
433 mitochondria showed a turn or fold of ~180°. Of the 41 looped regions identified, 75% lacked Mitotracker
434 staining. This suggests that mitochondria looped regions in *P. falciparum* have some degree of depolarization
435 that prevents Mitotracker accumulation or that Mitotracker initially accumulates in these regions but is not
436 bound and retained. The biological significance of these areas, if any, is currently unclear.

437 *Growth of the apicoplast and mitochondrion*

438 To visualize the apicoplast, we utilized a previously established cell line that expresses GFP fused to
439 the apicoplast transit peptide of acyl carrier protein (ACP)[56], which we will refer to as Apicoplast-GFP. This
440 marker allowed for a relatively even and continuous staining of the organelle. We quantified mitochondrion
441 and apicoplast signal area using ATPd-smHA and Apicoplast-GFP respectively as a proxy measurement of
442 size (Figure 5c&6b). Tracking this in parallel to parasite nucleus number allowed us to determine whether the
443 growth of these organelles occurred progressively with simultaneous rounds of mitosis and nuclear division.
444 In mononucleated ring and trophozoite parasites, both the mitochondria and the apicoplast are relatively small,
445 having an average area of 13.39 μm^2 (± 15.1 μm^2 SD) and 4.81 μm^2 (± 2.62 μm^2 SD) respectively in expanded
446 parasites (Supplementary Figure 6). As expected from live cell observations[45], both organelles show
447 significant growth and spread throughout the cell in multinucleated parasites, adopting an elongated and
448 branching morphology (Figure 5&6). Mitochondria grow almost exclusively during the first two rounds of
449 nuclear replication, achieving an average size of 87.9 μm^2 (± 15.9 μm^2 SD) at the 2-5 nuclei stage. This size
450 remains relatively constant until segmentation, with the average mitochondria size right before the start of
451 fission being 99.6 μm^2 (± 37.4 μm^2 SD) (Figure 5c). In contrast, the apicoplast continues to grow past the 2-
452 5 nuclei stage, having an average size of 25.5 μm^2 (± 7.21 μm^2 SD) at the 2-5 nuclei stage and 34.97 μm^2 (±
453 11.23 μm^2 SD) in cells with >15 nuclei (Figure 6b). These data suggest that the mitochondrion and apicoplast
454 do not grow simultaneously with or as a response to nuclear replication during schizogony. Rather, both
455 organelles show the largest increase in size during the 1 to 2 nuclei transition and either plateau in size, in the

456 case of the mitochondria, or enter a second phase of slower growth that ends shortly before segmentation, in
457 the case of the apicoplast.

458 *Fission of the mitochondrion and apicoplast*

459 *P. falciparum* has a single, large, branching, mitochondrion and apicoplast throughout most of the
460 asexual blood stage[45,46,57]. During segmentation, however, these organelles undergo fission such that each
461 merozoite inherits an individual apicoplast and mitochondrion[16,45]. While it has been shown that apicoplast
462 fission occurs before mitochondrial fission, it is unclear how fission occurs[16]. A recent review[57] posed three
463 possible mechanisms: synchronous fission where the organelle simultaneously divides into all daughter
464 parasites at once, outside-in fission where fission occurs at the ends of the organelle, or branching point fission
465 where a first fission event divides the organelle into larger segments and a subsequent fission event leaves
466 each merozoite with an individual organelle[57]. It also remains unclear how accurate segregation into daughter
467 cells is monitored. In *T. gondii*, the apicoplast associates with the centrosomes prior to undergoing fission. A
468 similar association between apicoplasts and MTOCs has been proposed in *Plasmodium* but still lacks evidence
469 due to the difficulty of observing the *Plasmodium* MTOC in live cells[45]. The mitochondrion is not thought to
470 associate with the MTOC in *Toxoplasma* or *Plasmodium* and its mechanism for ensuring accurate segregation
471 remains unknown.

472 In the process of imaging the mitochondria and apicoplasts of segmenting parasites, we observed a
473 transient MTOC association prior to and during fission in both organelles. Just before the start of segmentation,
474 there is little association between the MTOC and apicoplast. Of 5 parasites imaged that had >10 nuclei but
475 had not yet started segmentation, 3 had no contact points between the MTOC and apicoplast branches and the
476 other 2 had <4 contact points. Once segmentation starts, all apicoplast branches contact an MTOC each and
477 remain in contact with the MTOC until the end of apicoplast fission and MTOC degradation (Figure 6c). In
478 11 imaged segmenting schizonts, all MTOCs showed contact with an apicoplast branch each. This association
479 starts in early segmentation, when all MTOCs are connected by a single branched apicoplast. By the time the
480 basal complex reaches maximum diameter and begins contraction, we observe 7 parasites where all branches
481 have completed fission and 2 parasites that had at least one or more apicoplast segments still connecting
482 multiple merozoites (Figure 6c). Mitochondria fission follows a very similar pattern, but later in parasite

483 development. Prior to the basal complex reaching maximum diameter, we observe no significant connection
484 between the MTOC and mitochondria. When the basal complex entered its contraction phase, we observed 9
485 parasites where all MTOCs were in contact with one branch of the mitochondria each (Figure 5 d&e). Only
486 one of these 9 parasites had an intact pre-fission mitochondrion, while the other 8 had undergone at least one
487 fission event. Matching previous descriptions of mitochondria and apicoplast segmentation, C1-arrested
488 schizonts having completed segmentation show elongated mitochondria (Figure 5a) and small, rounded
489 apicoplasts (Figure 6a).

490 Both mitochondria and apicoplast fission showed neighbouring nascent merozoites that shared a single
491 branch of mitochondria or apicoplast passing through both of their basal complexes while others had an
492 individual mitochondrion or apicoplast which had already separated from the rest (Figure 5d&6c). This
493 suggests that fission does not occur synchronously (Figure 5d) and supports the model of branching point
494 fission. In other words, parasites seem to undergo a primary fission event that leaves only some merozoites
495 sharing stretches of the organelles and then a subsequent fission event leaves each merozoite with an individual
496 apicoplast and mitochondrion (Figure 5e). Unfortunately, BODIPY TRc does not distinctly stain the
497 membranes of the mitochondria and apicoplast. So, it is not possible for us to determine whether the observed
498 breaks in staining of our chosen organelle markers truly indicate a complete fission of the mitochondria or
499 apicoplast membranes. Thus, while suggestive of branching point fission, our data is not sufficient to
500 conclusively determine the sequence of fission events in these organelles.

501 *Characterisation of residual body mitochondria*

502 At the completion of segmentation, the parasite forms a structure known as the residual body, which
503 contains parasite material, such as the hemozoin crystal, that was not incorporated into merozoites during
504 segmentation[16]. The residual body is poorly understood in *Plasmodium*, but in *Toxoplasma* it has been shown
505 that a significant amount of the mitochondria, and not the apicoplast, is left behind in the residual body
506 following segmentation[58].

507

508

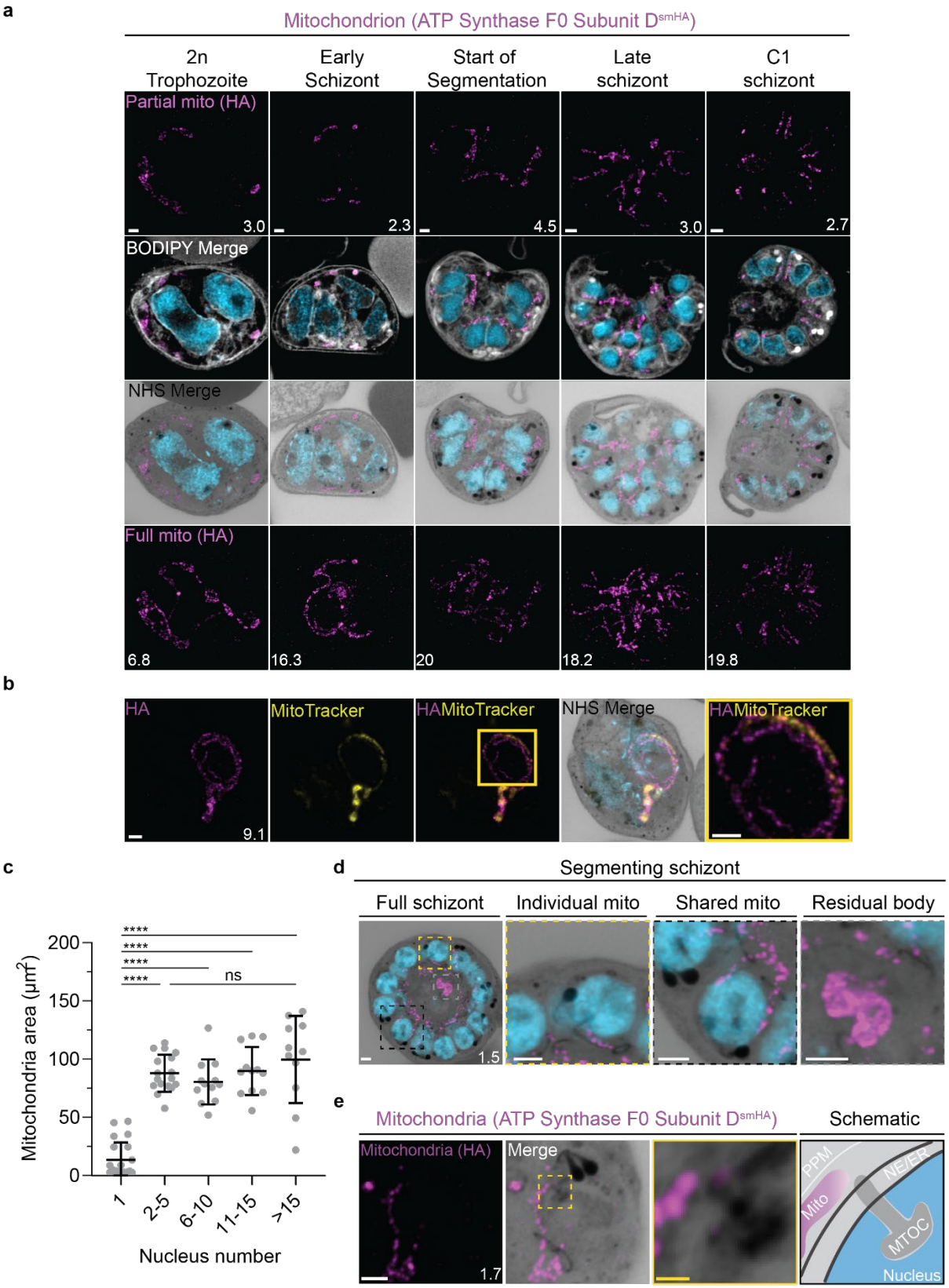

Figure 5: Growth and fission of the mitochondrion.
(a) *Parasites with an smHA-tagged copy of the ATP Synthase F0 Subunit D (ATPd, Pf3D7_0311800) as a mitochondrial marker were prepared by U-ExM, stained with NHS ester (greyscale), BODIPY TRc (white), SYTOX (cyan) and anti-HA (mitochondrion; magenta) antibodies and imaged using Airyscan microscopy across the asexual blood stage. Maximum intensity projections of both a subsection of the cell (partial mito) and the full cell (full mito) are shown.* ***(b)*** *ATPd staining was compared against Mitotracker orange CMTMRos (yellow), which showed discontinuous staining in looped regions.* ***(c)*** *Area of the mitochondrion was quantified for parasites of varying nucleus number. 73 cells were counted across 4 biological replicates. **** = $p<0.001$, ns = $p>0.05$ by one-way ANOVA, error bars = SD.* ***(d)*** *Schizont with mitochondria that have undergone fission (yellow zoom), mitochondria that are shared between two nascent merozoites (black zoom), and mitochondria left outside merozoites in the forming residual body (grey).* ***(e)*** *During fission, mitochondria associate with the cytoplasmic extension of the MTOC. Images are maximum-intensity projections, number on image = Z-axis thickness of projection in µm. White scale bars = 2 µm, yellow scale bars = 500 nm.*

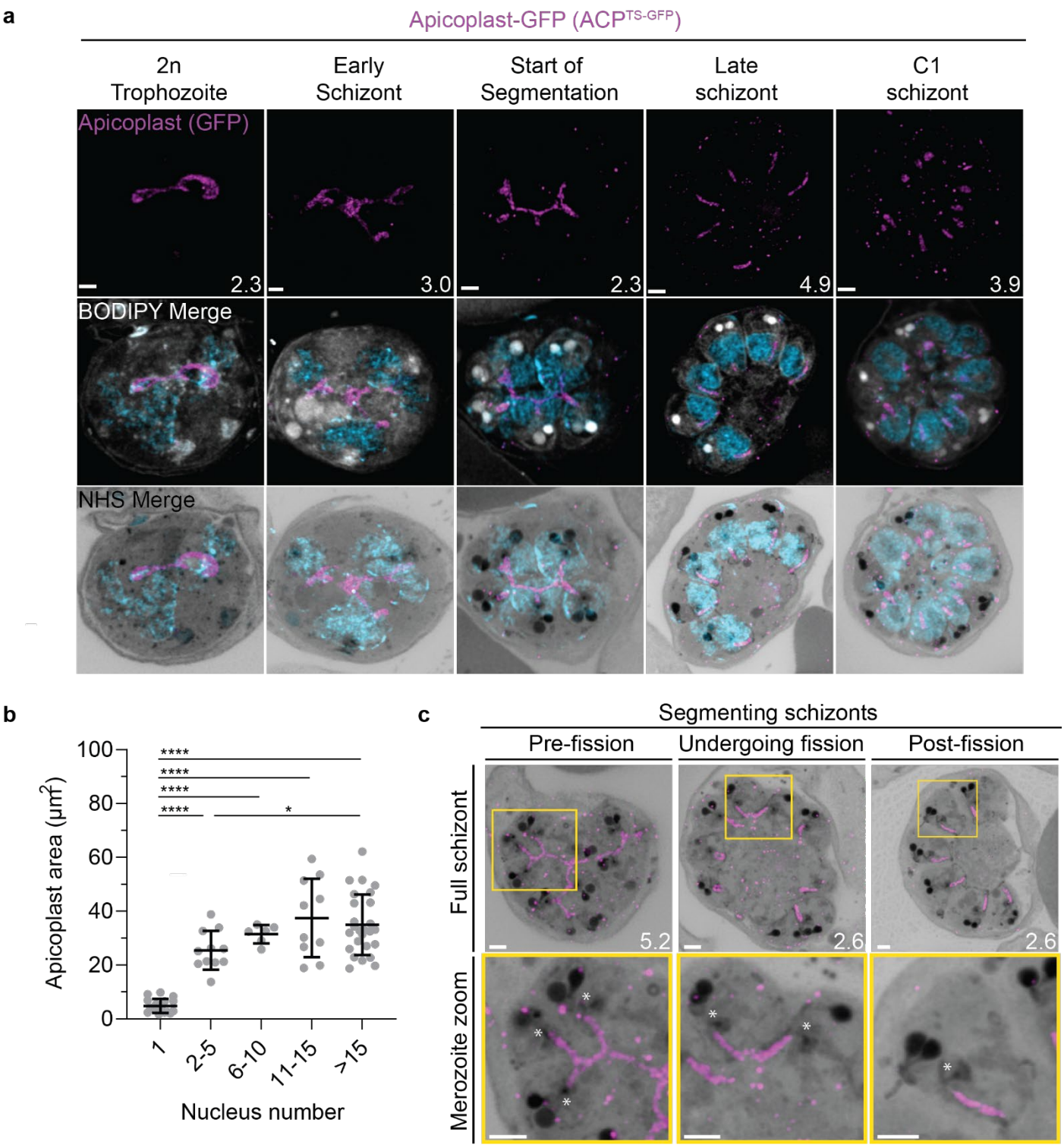

Figure 6: Growth and fission of the apicoplast.

(a) *Parasites expressing GFP-conjugated to the apicoplast transit signal of ACP (ACP$^{Ts\text{-}GFP}$) were prepared by U-ExM, stained with NHS ester (greyscale), BODIPY TRc (white), SYTOX (cyan) and anti-GFP (apicoplast) (magenta) antibodies and using Airyscan microscopy across the asexual blood stage.* ***(b)*** *Area of the apicoplast was quantified* for parasites of varying nucleus number. *70 cells were counted across 3 biological replicates.* **** = $p<0.001$, * = $p<0.05$ by one-way ANOVA, error bars = SD. ***(c)*** *Representative images of the different stages of apicoplast fission. Images are maximum-intensity projections, number on image = Z-axis thickness of projection in µm. Asterisks represent MTOCs. Scale bars = 2 µm.*

529 There is no well-characterized marker of the residual body in *Plasmodium*. So, for this study, we
530 defined the residual body as any area within the parasitophorous vacuole membrane but visibly external to
531 any merozoite in a C1-arrested schizont as determined by BODIPY TRc staining. We imaged 35 C1-arrested
532 schizonts and observed that 54% had mitochondrial staining inside the residual body (Figure 5d and
533 Supplementary Figure 9c). To determine the proportion of total mitochondria that gets included in the residual
534 body, we quantified the fluorescence of both mitochondria in the residual body and mitochondria in merozoites.
535 Of the 19 parasites that showed mitochondria staining inside the residual body, the amount of material ranged
536 from 1% to 12% of the total mitochondrial staining in the parasite (Supplementary figure 9d). On average, the
537 residual body had approximately 1.5x more mitochondrial staining than the average merozoite
538 (Supplementary Figure 9d). No significant apicoplast staining was ever observed in the residual body,
539 similarly to what has been reported for *Toxoplasma*[58].

540 **Cytostomes**

541 During its intraerythrocytic development, *P. falciparum* engulfs host cell cytoplasm from which it
542 catabolizes haemoglobin as a source of amino acids[59]. The parasite is separated from its host cell by the
543 parasitophorous vacuole, and therefore the uptake of host-cell cytosol requires invagination of both the PPM
544 and PVM. The cytostome coordinates this endocytic process and is comprised of two key regions: a protein-
545 dense collar region, which forms the pore through which membrane invagination will occur, and the
546 membranous bulb region, which contains the RBC-derived cargo[60,61].

547 *NHS ester staining reveals pore-like structures at the parasite plasma membrane.*

548 Prior to this study, cytostomes were not immediately obvious by NHS ester staining given the large number
549 of features that were visible using this stain but pending validation. While observing the basal complex of
550 segmenting schizonts (Figure 4), we noticed that merozoites contained a second NHS-ester-dense ring (Figure
551 4b and Figure 7a). The size and position of this NHS ester ring matched that of an endocytic micropore recently
552 identified in *Toxoplasma* tachyzoites[62]. In that study, the micropore was identified using Kelch13 (K13) as a
553 marker [62]. To investigate whether this NHS-ester-dense ring was indeed the K13 micropore, we evaluated a
554 parasite strain where the endogenous K13 was fused to GFP[63]. Investigation using this parasite line revealed

555 that the NHS-ester-dense ring also stained with K13, suggesting that this structure is an endocytic micropore
556 (Figure 7b). Furthermore, K13-stained micropores were detected at all stages of the parasite lifecycle (Figure
557 7c). Ring-stage parasites typically contained one or two micropores, which increased in number during the
558 trophozoite stage and schizogony (Figure 7c).

559 Single cytostomes appear in the area containing the IMC near the apical organelles at the same time as the
560 basal complex forms a complete ring. Cytostomes remain within the IMC area but change positions within
561 the nascent merozoite as segmentation progresses (Figure 4b, white asterisks). The majority of merozoites in
562 C1-arrested schizonts contained a single cytostome. This suggests that cytostomes are incorporated into the
563 IMC of merozoites and inherited early in segmentation. Clusters of cytostomes that had not been incorporated
564 into merozoites during segmentation were observed either adjacent to nascent merozoites or as part of the
565 residual body (Supplementary Figure 11 and Figure 4b, yellow asterisk). It is currently unclear whether there
566 are any functional differences between the cytostomes that are incorporated into merozoites and those that are
567 left behind.

568 *The observed micropore is the cytostome collar.*

569 K13 should localize to the collar of cytostomes when the parasite is performing endocytosis[64]. While
570 many K13-positive micropores were present at the lifecycle stages when endocytosis is expected (Figure 7c),
571 they were not attached to cargo-containing, protein-dense bulbs indicative of active endocytosis[61].
572 Occasionally, K13-micropores were attached to membranous structures visible either by BODIPY TRc
573 staining (Figure 7d) or by a decrease in NHS ester staining (Supplementary Figure 11), but these did not match
574 the density or complexity suggested by electron microscopy studies of the same structures. Fixation using 4%
575 v/v paraformaldehyde (PFA) is known to result in the permeabilization of the RBC membrane and loss of its
576 cytoplasmic contents[65]. Topologically, the cytostome is contiguous with the RBC cytoplasm and so we
577 hypothesised that PFA fixation was resulting in the loss of cytostomal contents and obscuring of the bulb.
578 PFA-glutaraldehyde fixation has been shown to better preserve the RBC cytoplasm[65]. So, we prepared samples
579 using this fixative and observed large protein-dense cytostome bulbs (Figure 7e). Collectively, this data
580 supports the hypothesis that these NHS-ester-dense rings are indeed cytostomes and that endocytosis can be
581 studied using U-ExM, but PFA-glutaraldehyde fixation is required to maintain cytostome bulb integrity.

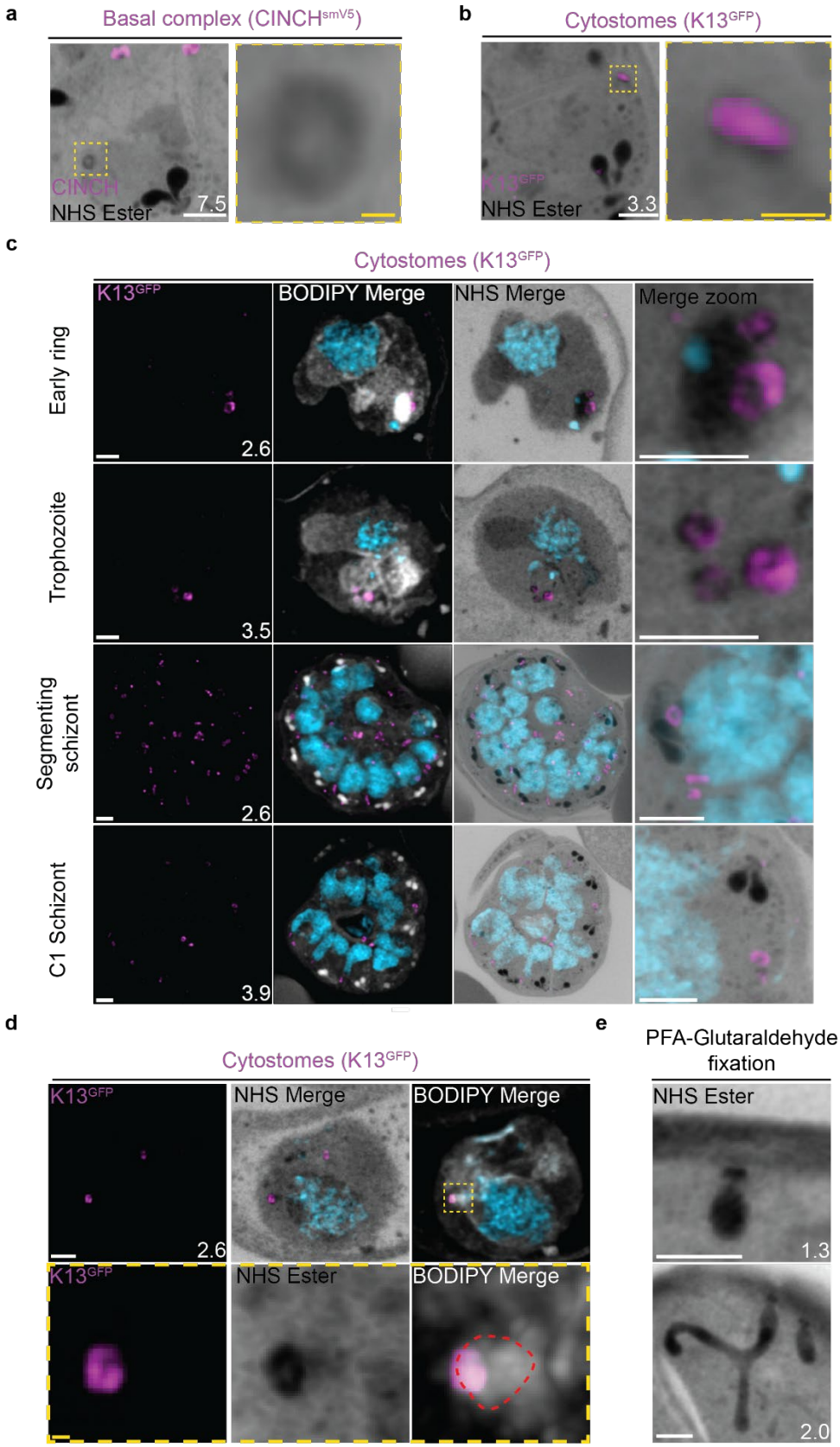

Figure 7: Cytostomes are observable by U-ExM throughout the asexual blood stage of the lifecycle. ***(a)*** *Parasites expressing an smV5-tagged copy of the basal complex marker CINCH and stained anti-V5, show NHS ester dense rings that are negative for this basal complex marker.* ***(b)*** *Parasites where the cytostome marker Kelch13 was conjugated to GFP (K13-GFP), showed overlap between K13 and this non-basal complex structure when stained against GFP.* ***(c)*** *K13-GFP parasites were prepared by U-ExM, stained with NHS ester (greyscale), BODIPY TRc (white), SYTOX (cyan) and anti-GFP (Cytostome) (magenta) antibodies and imaged using Airyscan microscopy across the asexual blood stage.* ***(d)*** *Paraformaldehyde (PFA) fixed parasites and zoom into region marked by yellow dotted line. Red dotted line marks example of a vesicle attached to the cytostome collar occasionally visible by NHS ester or BODIPY.* ***(e)*** *In PFA-glutaraldehyde fixed samples, cytostome collars were attached to protein-dense bulb regions. Images are maximum-intensity projections, number on image = Z-axis thickness of projection in µm. White scale bars = 2 µm. Yellow scale bars = 500 nm.*

592 *Non-canonical cytostome collar morphologies*

593 We noticed a number of different cytostome morphologies and organizational patterns (Supplementary
594 Figure 11). Cytostomes frequently clustered together and did not appear randomly distributed across the PPM
595 (Figure 7c). Some cytostomes would form what appeared to be higher order structures where two or three
596 distinct cytostomal collars appeared to be stacked end-on-end (Supplementary Figure 11). Cytostomes have a
597 relatively well defined and consistent size[64,66], but occasionally we observed very large cytostomal collars that
598 were approximately twice the diameter of other cytostome collars in the same cell (Supplementary Figure 11).
599 It is unclear what the function of these higher order structures or large cytostomes is, if they represent
600 biogenesis transition states, or indeed if they're performing some specialized endocytosis.

601

602 **The rhoptries**

603 To invade host red blood cells, merozoites secrete proteins from specialized secretory organelles
604 known as the rhoptries and micronemes. While both the rhoptries and micronemes are well studied in the
605 context of *Plasmodium* biology, neither have been investigated in detail using expansion microscopy in
606 *Plasmodium*. We previously showed that fully formed rhoptries can be observed by NHS ester staining alone[6],
607 but did not investigate their biogenesis.

608 *Rhoptries can be observed from early in their biogenesis using NHS ester staining.*

609 Rhoptries consist of a neck and bulb region, with the tip of the neck being loaded into the apical polar
610 rings of merozoites. Despite both being formed from Golgi-derived cargo, the neck and bulb regions have
611 distinct proteomes[26]. We first tracked rhoptry bulb biogenesis across schizogony using antibodies directed
612 against the rhoptry bulb marker rhoptry associated protein 1 (RAP1).

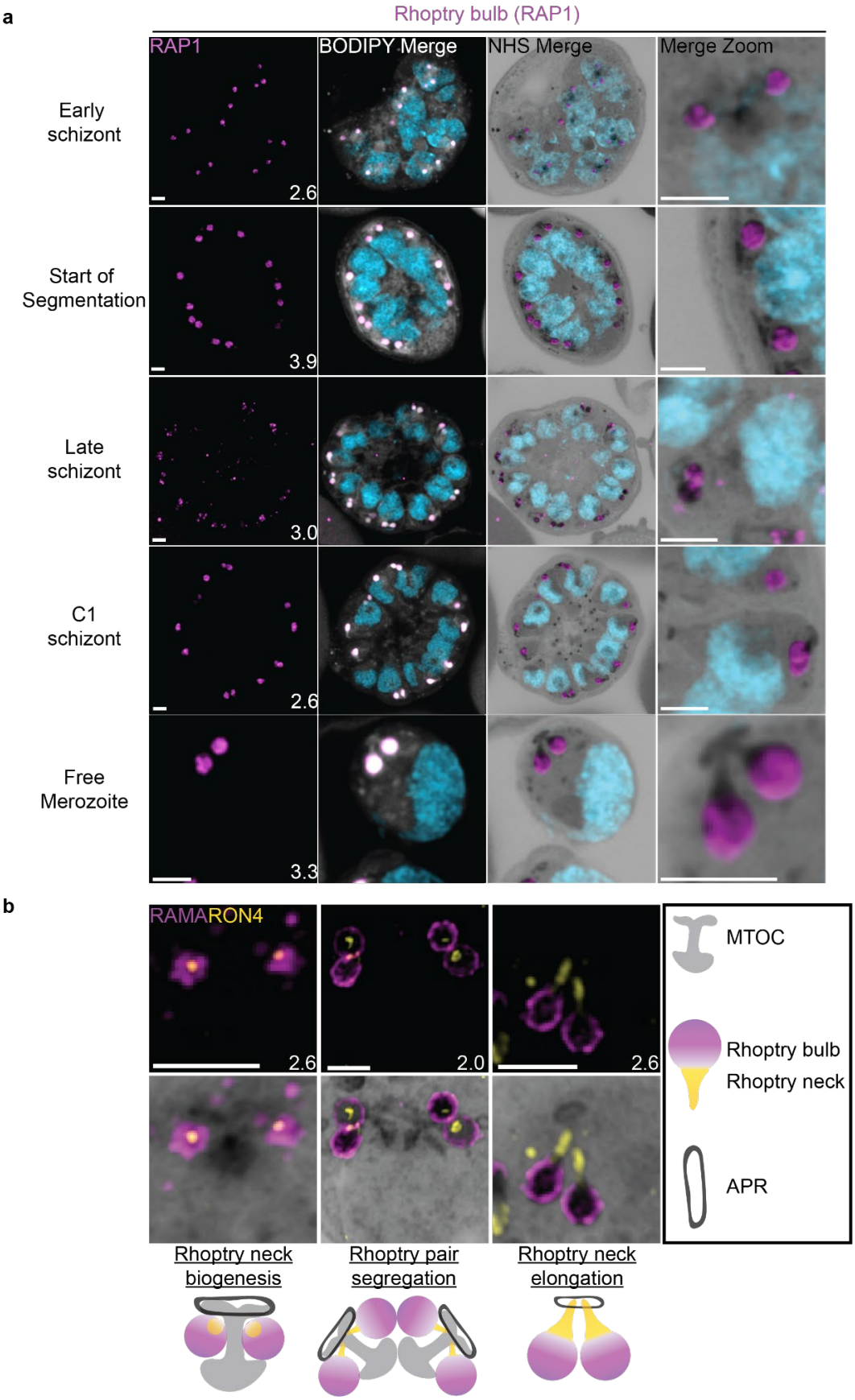

Figure 8: Rhoptries undergo biogenesis near the MTOC and are segregated during nuclear division.
(a) *3D7 parasites were prepared by U-ExM, stained with NHS ester (greyscale), BODIPY TRc (white), SYTOX (cyan) and anti-RAP1 (rhoptry bulb; magenta) antibodies and imaged using Airyscan microscopy throughout schizogony.* ***(b)*** *3D7 parasites were stained with NHS Ester (greyscale) along with antibodies against RAMA (rhoptry bulb; magenta) and RON4 (rhoptry neck; yellow) to assess rhoptry enck biogenesis. We observed that the rhoptry neck begins as a single focus inside each rhoptry. Rhoptries then get duplicated and segregated alongside the MTOC. During the final mitosis, the rhoptry neck begins to elongate and the rhoptries separate from MTOC. Images are maximum-intensity projections, number on image = Z-axis thickness of projection in µm . Scale bars = 2 µm.*

622 Nascent rhoptries were detected early in schizogony, with RAP1 foci appearing adjacent to all MTOC
623 cytoplasmic extensions from parasites with 6-10 nuclei in a one-to-one ratio, as described above (Figure 8a
624 and Supplementary Figure 12b). These foci co-localized with NHS ester densities of the same size and round
625 shape, no elongated neck-like structures were visible by NHS ester (neck biogenesis described in more detail
626 below). This matches reports that rhoptry bulb biogenesis occurs first[26,67], with neck biogenesis not occurring
627 until segmentation. As early as the last mitotic event during early segmentation, rhoptry bulbs were observed
628 as pairs, with 88 of 93 (95%) MTOCs observed forming a mitotic spindle being associated with two RAP1-
629 positive NHS ester densities per MTOC cytoplasmic extension. Finally, in newly invaded ring-stage parasites,
630 strong RAP1 staining was observed at the PPM/PVM (Supplementary Figure 12a), supporting previously
631 reported observations that secreted RAP1 coats the merozoite during invasion[68].

632 Our data not only suggests that rhoptry biogenesis occurs well before segmentation, when nuclei still have
633 several rounds of mitosis to complete, but also that rhoptries remain MTOC-associated during these mitotic
634 events. Instances of this association with the MTOC have been observed before[16,67] but its mechanism remains
635 unknown. To our knowledge, this is the first in-depth documentation of a rhoptry-MTOC association
636 throughout schizogony in *Plasmodium*.

637 *Rhoptry heterogeneity during early schizogony and segmentation.*

638 Rhoptries associated with the same MTOC during early schizogony sometimes differ in size
639 (Supplementary Figure 12b). This is not surprising given the speed of mitotic events requires near-constant
640 biogenesis of new rhoptry bulbs. By the time segmentation is underway, instead of inheriting one sister rhoptry
641 in the final mitotic event of schizogony, each MTOC will inherit a pair of rhoptries each. At this point, the
642 speed of these mitotic events slows and parasites reach a point of semi-synchrony. To our surprise, this
643 synchrony does not extend to rhoptry pairs and the two rhoptries inherited by segmenting daughter cells remain
644 different from each other. This heterogeneity in rhoptry pairs during early segmentation has been documented
645 before by electron microscopy[16,67]. Of 109 rhoptry pairs imaged in early segmentation schizonts undergoing
646 their last miotic event (where MTOCs were observed forming mitotic spindles), only 4% had two rhoptries of
647 similar size and density (Supplementary Figure 12d). We observed that 40% of these 109 rhoptry pairs had
648 different size but equal NHS ester density, 21% had the same size but different NHS ester density, and 35%

649 differed in both size and NHS ester density (Supplementary Figure 12e). As expected from previous reports,
650 this heterogeneity was lost after the completion of this last miotic event and rhoptry neck elongation. Of 98
651 rhoptry pairs imaged in non-mitotic segmenting parasites, 76% had two rhoptries of similar size and density
652 (Supplementary Figure 12d). Overall, these observations of heterogeneity support the hypothesis that rhoptry
653 pairs undergo independent biogenesis rather than splitting off from a single precursor rhoptry. However, it is
654 still unclear how the one-to-two rhoptry transition occurs and whether this heterogeneity has a biological role
655 in rhoptry biogenesis and maturation or whether it is simply an indicator of maturity and a by-product of
656 sequential rhoptry biogenesis.

657 These observations support a model where rhoptries undergo sequential segregations alongside the
658 MTOC and a second rhoptry forms *de novo* after each segregation event. This process would repeat until the
659 start of segmentation and formation of rhoptry pairs. Constant *de novo* biogenesis could explain why one
660 rhoptry can appear smaller or less mature than the other[16,67]. It is currently unclear, however, why
661 heterogeneity in rhoptry density only appears during early segmentation and not earlier, when biogenesis of
662 new rhoptries is arguably more apparent. Thus, this model is not enough to explain all the variation in rhoptry
663 size and density observed throughout schizogony. Furthermore, a lot of unknowns remain about what exactly
664 governs rhoptry number during the rapid rounds of asynchronous nuclear division[69], how the transition to a
665 rhoptry pair is signalled, and how many rounds of *de novo* rhoptry formation parasites undergo.

666 *Rhoptry neck biogenesis and elongation*

667 In order to observe rhoptry neck biogenesis in more detail, we stained parasites against the rhoptry apical
668 membrane antigen (RAMA, a rhoptry bulb marker) and rhoptry neck protein 4 (RON4, a rhoptry neck
669 marker)[70,71]. RAMA is anchored to the rhoptry bulb membrane and only stains the periphery of the rhoptry
670 bulb as marked by NHS ester (Figure 8b and Supplementary Figure 12c). RON4 is absent from the earliest
671 rhoptry bulbs, appearing as a focus within the rhoptry bulb shortly before early segmentation and before the
672 rhoptry neck could be distinguished from the bulb by NHS ester staining alone (Figure 8b). During early
673 segmentation, when rhoptry pairs first become visible, we observe an uneven distribution of RON4 within
674 each pair. RON4 preferentially associates with one of the rhoptries, with the staining on the second rhoptry
675 being fainter, more diffuse, or even absent in some cases. Of 84 rhoptry pairs observed at this stage, 72 (86%)

676 showed an uneven distribution of RON4. To our surprise, when these rhoptry pairs were of different NHS
677 ester densities, the larger share of RON4 associated with the less dense rhoptry (Figure 8b). Previous
678 observations of rhoptry density differences by electron microscopy have been ascribed to differences in
679 rhoptry age or maturity, with the denser rhoptry being more mature. So, finding RON4 to be more abundant
680 in the less dense rhoptry suggests that either heterogenous RON4 accumulation cannot be explained by rhoptry
681 age or that the less dense rhoptry is instead the older rhoptry. The RON4-positive rhoptry neck elongates
682 during segmentation, attaining its characteristic shape by mid to late segmentation and becoming observable
683 by both RON4 staining and NHS ester (Figure 8). At this point, nearly all rhoptry necks had an equal
684 distribution or RON4. Of 76 rhoptry pairs observed at these stages, 72 (95%) had an equal distribution of
685 RON4.

686 **The micronemes**

687 Previous studies have suggested that micronemes may be heterogeneous and that apical membrane
688 antigen 1 (AMA1) and other micronemal markers such as erythrocyte binding antigen-175 (EBA175) reside
689 in different subsets of micronemes[72-74]. We reasoned that individual micronemes may be visible using U-ExM
690 and imaged parasites stained with AMA1 and EBA175 to observe their biogenesis and relative distribution.
691 The first microneme marker to appear during schizogony was AMA1. Large puncta of AMA1 appear near the
692 rhoptries when the basal complex is at its maximum diameter (Figure 9a). At this point, EBA175 is not yet
693 detectable above background fluorescence. At the end of segmentation, we observe AMA1 has arranged itself
694 into small, densely arranged puncta below the APR and around the rhoptry neck. We also observe EBA175
695 staining in puncta of the same size that are less densely arranged and have little co-localization with AMA1.
696 EBA175 puncta are basal to the AMA1 puncta, being closer to the rhoptry bulb. They also form a cloud of
697 larger diameter than the one formed by AMA1 such that, when viewed from above the APR, two concentric
698 clouds are observed with the core being AMA1 positive and the periphery being EBA175 positive (Figure
699 9b&c). The AMA1 and EBA175 staining we observed in late-stage schizonts partially overlaps with a punctate
700 NHS-ester pattern, suggesting that NHS-ester stains the micronemes (Figure 9b). However, many NHS-ester-
701 positive foci did not stain with either AMA1 or EBA175 despite being morphologically indistinguishable from
702 those which did. This suggests that NHS-ester stains more than just the micronemes and that some of these

703 foci may be exonemes, dense granules, or other apical vesicles. Alternatively, it is also possible that these
704 additional NHS-ester-positive foci represent micronemes that lack both AMA1 and EBA175.

705 Using the protease inhibitor E64, we arrested parasites "post-egress" such that AMA1 was translocated.
706 E64 allows for normal daughter cell maturation but prevents RBC plasma membrane rupture once
707 segmentation is complete[75]. We observe that once AMA1 is translocated, the density of apical AMA1
708 decreases. EBA175, which does not translocate, increases in density, and moves apically, taking the space
709 AMA1 occupied prior to translocation (Figure 9b&c). This is consistent with existing models of sequential
710 microneme translocation and microneme fusion near the APR[76].

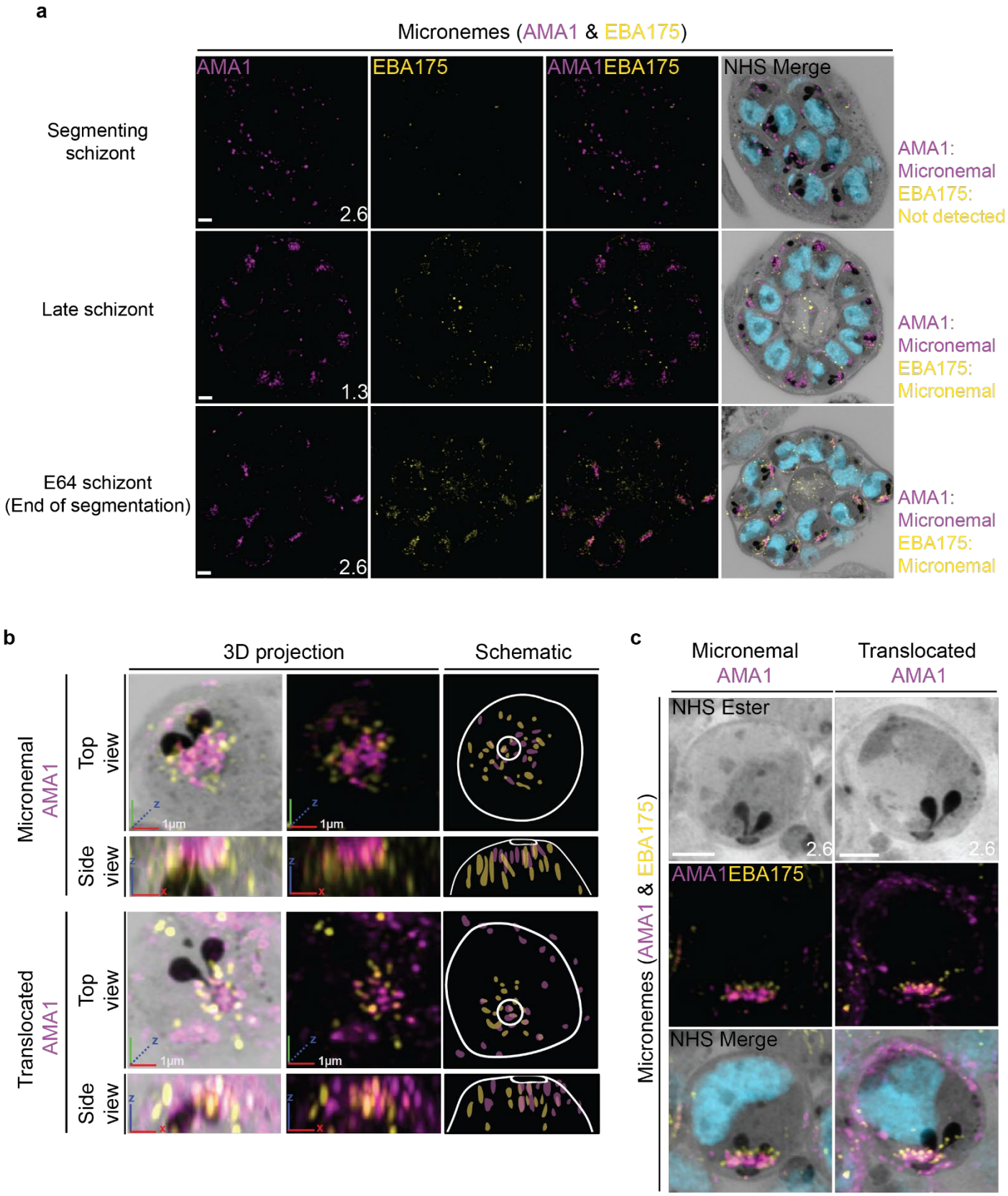

Figure 9: Micronemal proteins AMA1 and EBA175 reside in separate micronemes.
(a) *3D7 parasites were prepared by U-ExM, stained with NHS ester (greyscale), SYTOX (cyan) and antibodies against the micronemal markers AMA1 (magenta) and EBA-175 (yellow), and imaged using Airyscan microscopy in segmenting schizonts. In schizonts still undergoing segmentation, AMA1 localized to the apical end while EBA175 was not detected. In late schizonts, both EBA175 and AMA1 were present in the micronemes. In E64-arrested schizonts, AMA1 was translocated to the merozoite surface while EBA175 remained micronemal. 3D rendering* ***(b)*** *and zooms* ***(c)*** *of merozoites with either micronemal or translocated AMA1. Foci of AMA1 and EBA175 to not routinely colocalize with each other. Images are maximum-intensity projections, number on image = Z-axis thickness of projection in µm. White scale bars = 2 µm, RGB scale bars for 3D rendering = 1 µm.*

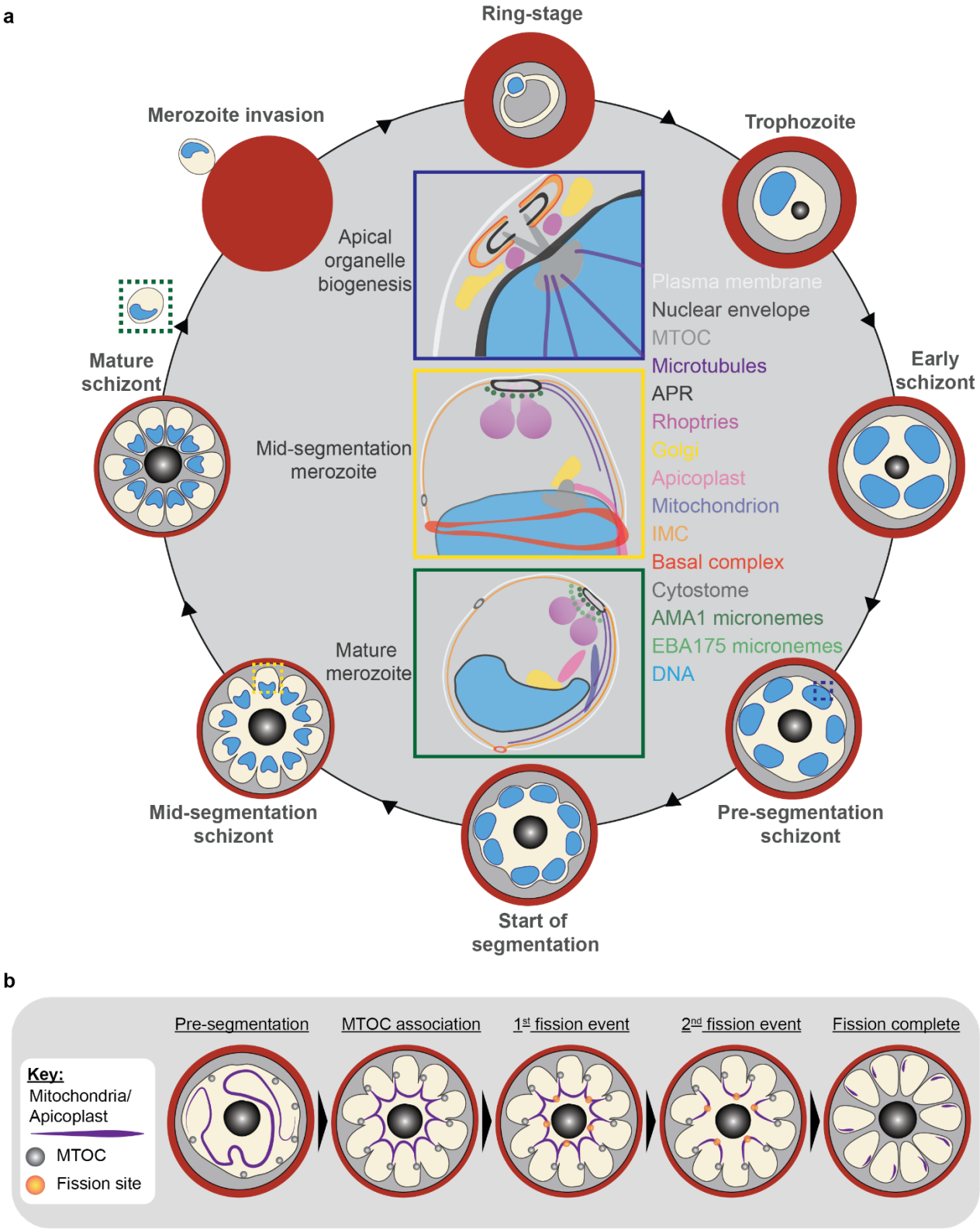

Figure 10: Summary of organelle organization and fission during schizogony.
(a) *Apical organelle biogenesis: Biogenesis of the rhoptries, Golgi, basal complex, and apical polar rings occur at the cytoplasmic extensions of the nuclear MTOC, between the nuclear envelope and parasite plasma membrane. Duplication and segregation of these organelles appears to be tied to MTOC duplication and segregation following nuclear divison. Mid-segmentation merozoite: The rhoptry neck is distinguishable from the bulb, and AMA1-positive micronemes are present at the apical end of the forming merozoite. Each merozoite has inherited a cytostome. Subpellicular microtubules stretch the entire distance from the apical polar rings and the basal complex. The apicoplast has attached to the nuclear MTOC and begun fission. Mature merozoite: The parasite has completed segmentation, and each merozoite contains a full suite of organelles. The nuclear MTOC is no longer visible, and EBA175-positive micronemes are both visible and separate from AMA1-positive micronemes.* ***(b)*** *Model for fission of the mitochondrion and apicoplast. Prior to fission, both the apicoplast and mitochondrion branch throughout the parasite cytoplasm, before associating with the MTOC of each forming merozoite. For the apicoplast, this occurs during the final mitosis, but not until late in segmentation for the mitochondrion. Following MTOC association, the apicoplast and mitochondrion undergo a first fission event, which leaves an apicoplast and mitochondrion shared between forming merozoite pairs. Subsequently both organelles undergo a second fission event, leaving each forming merozoite with a single apicoplast and mitochondrion.*

735 DISCUSSION

736 In this work, we apply U-ExM to the asexual blood stage of *Plasmodium falciparum* to provide new
737 insights into the role of the MTOC in establishing apical-basal polarity and in coordinating organelle
738 segregation during schizogony. In the process, we demonstrate U-ExM can be used to study the biogenesis
739 and protein distribution of a variety of organelles and structures within the parasite. Globally, our observations
740 suggest that the MTOC is involved in establishing apical-basal polarity within the parasite and that this polarity
741 is established early in schizogony.

742 We show that the cytoplasmic extensions of the MTOC appear to act as physical 'tethers', connecting
743 the nucleus to parasite plasma membrane (PPM). This creates a space between the PPM and nuclear envelope
744 where we observe multiple parasite structures and organelles including the Golgi, basal complex, rhoptries,
745 and apical polar rings. These structures and organelles remain MTOC-associated despite the constant
746 movement and segregation of MTOCs during mitotic events. Put together, these structures define the apical
747 end of the merozoite. In other systems, MTOC positioning has been described as a source of cellular polarity,
748 polarizing a cell by directing cargo of secretory organelles to a defined area [77-79]. While this has not been
749 previously described in *Plasmodium*, this model fits well with our observation of the Golgi being adjacent to
750 the MTOC throughout schizogony. This Golgi positioning could also perhaps provide a region of local
751 cytoplasmic exclusion that promotes biogenesis of rhoptries, micronemes, dense granules, and IMC, which
752 are all at least partially formed by Golgi-derived cargo[26,76,80,81]. While the biogenesis of the apical polar rings
753 seems to also be coupled to the MTOC, we do not yet know how they are nucleated or whether they are also
754 dependent on Golgi-derived cargo.

755 This study also shows MTOC-coupled organelle segregation and biogenesis to an extent never
756 observed before. Specifically, we observe that the Golgi, rhoptries, and basal complex match the MTOC
757 cytoplasmic extensions in number throughout early schizogony and segregate with MTOCs during the mitotic
758 events of schizogony. As this study used fixed cells, we lack the temporal power to precisely define the order
759 of these events. Using known markers of parasite age, however, we describe putative transition states that
760 nascent rhoptries and basal complexes adopt when being segregated with MTOCs. We put forward a model
761 where cytoplasmic MTOC-associated events occur before intra-nuclear MTOC-associated events. That is, the

762 duplication of the MTOC cytoplasmic extension and organelles precedes MTOC duplication and the formation
763 of a mitotic spindle such that this cytoplasmic duplication represents the first identifiable step in the
764 commitment of a nucleus to the next round of mitosis. Interestingly, nuclei can sometimes have MTOCs
765 forming a mitotic spindle that have already committed to the next round of mitosis by duplicating their
766 cytoplasmic cargo. That is, a mitotic nucleus can show four cytoplasmic extensions and sets of apical
767 organelles at the same time. While this supports our hypothesis that duplication of apical organelles and
768 cytoplasmic MTOC components happens upstream from intra-nuclear mitotic events, it does not tell us how
769 this relates to the genome copy number inside the nucleus. So, we cannot say whether DNA replication and
770 associated checkpoints occur upstream or downstream from the cytoplasmic events that seem to commit an
771 MTOC to mitosis.

772 Lastly, we contribute important evidence toward hypotheses across several open questions regarding
773 organelle biogenesis and segregation in *Plasmodium*. We observe contacts between the MTOC and both the
774 mitochondria and apicoplast during fission that suggest a role for this structure in monitoring copy number of
775 these organelles. We also document sequential fission events in both the apicoplast and mitochondria that are
776 suggestive of branching point fission. Lastly, we see temporal and spatial localization patterns of AMA1,
777 EBA175, and RON4 that support theories of heterogeneity within the apical organelles.

778 U-ExM represents an affordable and adaptable sample preparation method that can be applied to any
779 microscope to produce images with far greater visible detail than conventional light microscopy platforms.
780 Applying this technique to the visualization of organelle biogenesis and segregation throughout schizogony
781 allowed us to observe these processes in the context of structures that could previously only be investigated
782 in detail using electron microscopy. The flexibility and scalability of this technique allowed us to image more
783 than 600 individual parasites at a variety of developmental stages, increasing the confidence of our
784 observations and giving them some temporal resolution. To our knowledge, this paper represents the most
785 comprehensive study of a single organism using U-ExM, with a total of 13 different subcellular structures
786 investigated.

787 Our inability to pinpoint the nucleation site of the SPMTs or resolve the plasma membrane from the
788 IMC highlights some of the limitations of U-ExM as applied in this work. The subpellicular network that holds

789 IMC1g and lines the cytoplasmic face of the IMC sits approximately 20 nm below the parasite surface, where
790 we would find MSP1[82]. Thus, the distance between IMC1g and MSP1 post-expansion is around 90nm. This
791 is below our imaging resolution with Airyscan2, and close to the maximum resolution we could achieve
792 through other super-resolution methods compatible with our current setup when antibody effects are
793 considered. Thus, some parasite structures remain beyond the resolution achieved in this study. In order to
794 resolve the IMC from the plasma membrane or resolve multiple apical polar rings using light microscopy, we
795 would need to employ single molecule localization microscopy or iterative expansion microscopy[83], which
796 increases expansion factor to ~20x.

797 We also noticed some drawbacks and artifacts introduced by U-ExM. Most visually striking was that
798 the hemozoin crystal of the food vacuole does not expand[84], which leaves a large space that lacks NHS ester
799 staining in the center of the parasite. For nearly all antibodies used in this study, significant off-target
800 fluorescence was observed inside the food vacuole. Thus, U-ExM may not be as useful for studying food
801 vacuole biology. Occasionally, significant SYTOX (DNA stain) fluorescence was observed at either the
802 nuclear envelope or parasite plasma membrane. It is unclear if this represents an expansion-induced artifact
803 or a PFA-fixation artifact that is only now observable. Lastly, for cells stained with Mitotracker, some non-
804 specific background was observed that seemed to correlate with protein density as observed by NHS-ester.

805 Malaria parasites have been extensively studied using electron microscopy to determine their
806 ultrastructure and live-cell microscopy to observe their most dynamic processes in real time. Much of what
807 we uncovered in this study involved dynamic processes that are too small to be resolved using conventional
808 live-cell microscopy. Specifically, we made important observations about *P. falciparum* organelle biogenesis
809 and the organization of *Plasmodium* cell division around the MTOC. Rather than a replacement for any
810 existing microscopy techniques, we see U-ExM as a complement to the suite of techniques available to study
811 the cell biology of malaria parasites, which bridges some of the limitations of electron microscopy and live-
812 cell microscopy. As such, there are many parasite processes that are logical candidates for investigation by U-
813 ExM. Some of these have been highlighted in this paper, but others remain completely unexplored. Merozoite
814 invasion, for example, has been well-studied using a variety of microscopy techniques[31,68,85-87], but U-ExM
815 would allow us to visualise how all the apical organelles associate with each other and rearrange in three-

816 dimensions across the established time-course[86] of this process. Another logical candidate for investigation by
817 U-ExM is the rapid disassembly of the IMC and other merozoite organelles immediately following invasion[88],
818 a process where the parasite undergoes rapid and dramatic morphological rearrangements that lie beyond the
819 resolution of live-cell microscopy.

820

821 MATERIALS AND METHODS

822 ***Plasmodium falciparum* culture**

823 Unless otherwise stated, all parasites in this study were 3D7-Cas9[41]. For imaging of the apicoplast, the
824 previously generated ACP-transit-peptide-GFP cell line was used [56]. For imaging of Kelch13, the previously
825 generated 2xFKBP-GFP-K13 parasites were used[63].

826 All parasites were cultured in O^+ human red blood cells at 4% haematocrit in RPMI-1640 containing
827 25 mM HEPES, 50 mg/L hypoxanthine and 0.5% w/v Albumax II [89]. All parasite cultures were incubated on
828 a shaker at 37 °C in a gas mixture of 1% O_2, 5% CO_2, and 94% N_2 as previously described. The smHA-tagged
829 Pf3D7_0311800 (ATP Synthase F0 Subunit D) cell line was maintained under selection of 5 nm WR99210.
830 Apicoplast targeting signal-GFP line was maintained under selection of x mm x. 2xFKBP-GFP-K13 parasites
831 were maintained under selection of 0.9 µm DSM1.

832 Parasites were routinely synchronised using sorbitol lysis. Briefly, parasite cultures were resuspended
833 in 5% w/v D-sorbitol, resulting in the selective lysis of schizont-stage parasites[90].

834 For samples where parasites were arrested as schizonts using either trans-Epoxysuccinyl-L-
835 leucylamido(4guanidino)butane (E64)[91] or compound 1 (C1)[92], late schizont-stage cultures were treated with
836 either 10 µm E64 for ~3h or 5 µm C1 for ~5 hours.

837 **Plasmid generation and transfection**

838 For imaging of the mitochondria, a cell line where ATP-Synthase F0 Subunit D (Pf3D7_0311800) had a
839 C-terminal spaghetti-monster HA tag[35] was generated (Supplementary Figure 10). To create the
840 Pf3D7_0311800 smHA HDR plasmid, the 3D7_0311800 5' and 3' homology regions were PCR amplified

841 from 3D7 genomic DNA with oligonucleotides oJDD4893/oJDD4894 and oJDD4891/oJDD4892,
842 respectively. The two pieces were fused together using Sequence Overlap Extension PCR (SOE PCR) using
843 oJDD4891/oJDD4894 and the piece was digested with NotI/XhoI and ligated with T4 ligase to generate
844 pSAB55. To create the PF3D7_0311800 targeting guide RNA plasmid, oJDD4889/oJDD4890 were annealed,
845 phosphorylated, and ligated into BpiI-digested pRR216 to generate pSAB81. All oligonucleotide sequences
846 are shown in Supplementary Table 1.

847 For transfection, 100 µg of pSAB55 plasmid was linearized with StuI and transfected into 3D7-Cas9,
848 along with 100 µg of pSAB81. A day following transfection, parasites were treated with 5 nm WR99210 until
849 13 days, when resistant parasites were detected.

850 **Ultrastructure expansion microscopy**

851 Ultrastructure expansion microscopy (U-ExM) was performed as previously described with minor
852 modification[3,5,6]. 12 mm round Coverslips (Fisher Cat. No. NC1129240) were treated with poly-D-lysine for
853 1 h at 37 °C, washed twice with MilliQ water, and placed in the wells of a 12-well plate. Parasite cultures
854 were set to 0.5% haematocrit, and 1 mL of parasite culture was added to the well containing the coverslip and
855 for 15 min at 37 °C. Culture supernatants were removed, and cultures were fixed with 1 mL of
856 4% *v/v* paraformaldehyde (PFA) in 1xPBS for 15 min at 37 °C. For some experiments visualising cytostomes,
857 cultures were instead fixed in 4% v/v PFA + 0.01% v/v glutaraldehyde in 1xPBS. Following fixation,
858 coverslips were washed three times with 37 °C PBS before being treated with 1 mL of
859 1.4 % *v/v* formaldehyde/2% *v/v* acrylamide (FA/AA) in PBS. Samples were then incubated at 37 °C overnight.

860 Monomer solution (19% *w/w* sodium acrylate (Sigma Cat. No. 408220), 10% *v/v* acrylamide (Sigma Cat.
861 No. A4058, St. Louis, MO, USA), 2% *v/v* N,N'-methylenebisacrylamide (Sigma Cat. No. M1533) in PBS)
862 was typically made the night before gelation and stored at −20 °C overnight. Prior to gelation, FA/AA solution
863 was removed from coverslips, and they were washed once in PBS. For gelation, 5 µL of 10% v/v
864 tetraethylenediamine (TEMED; ThermoFisher Cat. No. 17919) and 5 µL of 10% *w/v* ammonium persulfate
865 (APS; ThermoFisher Cat. No. 17874) were added to 90 µL of monomer solution and briefly vortexed.
866 Subsequently, 35 µL was pipetted onto parafilm and coverslips were placed (cell side down) on top. Gels were

867 incubated at 37 °C for 30 minutes before being transferred to wells of a 6-well plate containing denaturation
868 buffer (200 mM sodium dodecyl sulphate (SDS), 200 mM NaCl, 50 mM Tris, pH 9). Gels were incubated in
869 denaturation buffer with shaking for 15 minutes, before separated gels were transferred to 1.5 mL tubes
870 containing denaturation buffer. 1.5 mL tubes were incubated at 95 °C for 90 minutes. Following denaturation,
871 gels were transferred to 10 cm Petri dishes to containing 25 mL of MilliQ water for the first round of expansion
872 and placed onto a shaker for 30 minutes three times, changing water in between. Gels were subsequently
873 shrunk with two 15-minute washes in 25 mL of 1x PBS, before being transferred to 6-well plates for 30
874 minutes of blocking in 3% BSA-PBS at room temperature. After blocking, gels were incubated with primary
875 antibodies, diluted in 3%BSA-PBS, overnight. After primary antibody incubation, gels were washed three
876 times in 0.5% v/v PBS-Tween 20 for 10 minutes before incubation with secondary antibodies diluted in 1x
877 PBS for 2.5 hours. Following secondary antibody incubation, gels were again washed three times in PBS-
878 Tween 20, before being transferred back to 10 cm Petri dishes for re-expansion with three 30-minute MilliQ
879 water incubations.

880 Gels were either imaged immediately following re-expansion, or stored in 0.2% w/v propyl gallate in
881 MilliQ water until imaging. For gels stained with BODIPY TR Ceramide, the fully expanded gel was
882 incubated overnight at room temperature in 0.2% w/v propyl gallate (Acos Organics Cat No. 131581000)
883 solution containing BODIPY TR ceramide (2 μM final concentration).

884 For parasites stained with Mitotracker Orange CMTMRos (ThermoFisher, M7510), parasite cultures
885 were resuspended in incomplete media + bicarb containing 300 nM Mitotracker Orange CMTMRos. Parasites
886 cultures were then stained with Mitotracker for 35 minutes while settling on Poly-D-lysine coated coverslips.
887 From this point, the expansion protocol was followed as described above, with the exception that all steps
888 when possible were carried out protecting the sample from light.

889 *Cryopreservation and thawing of gels.*

890 A proportion of gels imaged in this study were cryopreserved and subsequently thawed prior to
891 imaging[83]. Gels were frozen either unstained, following the first round of expansion, or frozen stained,
892 following the second round of expansion. To freeze, a portion of the expanded gel was placed into a 6-well
893 dish and washed three times with 50% glycerol in MilliQ water for 30 minutes. Fresh glycerol was then added,

894 and the gels were stored at -20 °C for future use. To thaw unstained gels, the glycerol was replaced with MilliQ
895 water and incubated at room temperature for 30 minutes. Gels were then washed and shrunk with three 20-
896 minute washes in 1x PBS at room temperature before proceeding with the antibody staining process normally.
897 Stained gels were thawed with three washes in MilliQ water for 30 minutes before proceeding with imaging
898 as normal.

899 **Stains and antibodies**

900 A comprehensive list of all stains and antibodies used in this study, their working concentrations, and
901 source(s) can be found in Supplementary Table 2.

902 **Image acquisition**

903 All images presented in this study were taken using either a Zeiss LSM800 AxioObserver with an
904 Airyscan detector, or a Zeiss LSM900 AxioObserver with an Airyscan 2 detector. Imaging on both
905 microscopes was conducted using a 63x Plan-Apochromat objective lens with a numerical aperture of 1.4. All
906 images were acquired as Z-stacks that had an XY pixel size of 0.035 µm and a Z-slice size of 0.13 µm.

907 **Image analysis**

908 *Image processing and presentation*

909 All images were Airyscan processed using 3D processing at moderate filter strength on ZEN Blue
910 Version 3.1 (Zeiss, Oberkochen, Germany).

911 The majority of images presented in this study are presented as z-projections for viewing purposes.
912 The majority of images are presented as maximum intensity projections, but those that contain BODIPY TR
913 Ceramide are presented as average intensity projections for viewing and interpretation purposes.

914 *3D rendering*

915 3D renderings of micronemal proteins AMA1 and EBA175 were produced using the 3D analysis
916 package on ZEN Blue version 3.5.

917 *Measurement of interpolar spindles and subpellicular microtubules*

918 All length measurements reported in this study were obtained using the "Measure 3D distance"
919 function of ZEN Blue Version 3.1. The length of Interpolar spindle microtubules and subpellicular
920 microtubules was determined as the 3D distance between the start and end points of continuously stained
921 stretches of anti-tubulin staining. Interpolar microtubules were defined as those whose staining appeared to
922 contact both MTOCs as defined by NHS ester, while non-interpolar microtubules were those that did not meet
923 these criteria. Subpellicular microtubules were only measured in C1-arrested schizonts that had visibly
924 completed segmentation based on the basal complex as visualised by NHS ester. Any microtubule that did not
925 appear connected to the apical polar ring, or extend towards the basal complex, was excluded from the analysis.
926 Cell diameter was defined as the greatest XY distance on any z-slice between two points of the parasite as
927 defined by NHS Ester staining. Merozoite length was defined as the 3D distance between the center of the
928 apical polar rings and basal complex as defined by NHS ester staining.

929 *Apicoplast and mitochondria area analysis*

930 All area measurements presented were obtained using the "Area" function on ZEN Blue Version 3.1.
931 Images were presented as a maximum intensity projection before free hand outlining the apicoplast or the
932 mitochondria in each image. The sum of all fragments was then calculated to find the total area of the
933 organelles per cell.

934 *Mitochondria residual body analysis*

935 In C1-arrested schizonts, the proportion of total mitochondria staining found in the residual body was
936 calculated as follows. Using ZEN Blue version 3.1, a maximum intensity projection of the entire cell was
937 generated and based on the NHS staining, the entire parasite was defined as the region of interest. Signal
938 intensity of the channel staining the mitochondria was calculated inside the full cell, which was defined as
939 total mitochondria fluorescence. Subsequently, the residual body was defined the area within the parasite
940 vacuole, but external to all merozoite plasma membranes, as based on BODIPY TR ceramide staining. A
941 second maximum intensity projection of this subsection of the schizont was made, the residual body was
942 defined as the region of interest and this signal intensity inside this region of interest was defined as residual
943 body mitochondria fluorescence.

944 To determine residual body mitochondria fluorescence (RB) as % total mitochondria fluorescence
945 (total), the following equation was used:

946 $$\left(\frac{RB\ fluorescence}{Total\ fluorescence}\right) \times 100$$

947 In each of the parasites included in this analysis, the number of merozoites was defined as the number
948 of distinct nuclei as determined by SYTOX staining. To determine residual body mitochondria fluorescence
949 as % of one merozoite, the following equation was used:

950 $$\left(RB\ fluorescence\ \div \left(\frac{Total\ fluorescence - RB\ fluorescence}{Number\ of\ merozoites}\right)\right) \times 100$$

951 Cells where no mitochondria fluorescence was visible inside the residual body, while visible inside
952 merozoites, were defined as having no residual body mitochondria. An attempt was made to do a similar
953 analysis on apicoplast stained cells, but no visible apicoplast staining was ever observed in the residual body.

954 **Statistical analysis**

955 *Estimation of actual distance from expanded samples*

956 Expansion factors for 43 gels used in this study were determined as follows. Gels were assumed to
957 have an initial diameter of 12 mm, as they are formed on a 12 mm diameter coverslip. Gels were subsequently
958 measured following expansion to the nearest whole millimetre, and the expansion factor was defined as the
959 expanded gel diameter divided by the initial gel diameter (12 mm). Gels whose edges were damaged or
960 malformed, and therefore their diameters could not be actually measured, were excluded. Gels in this study
961 had a median expanded diameter of 51 mm, which corresponds to a median expansion factor of 4.25
962 (Supplementary Figure 7)

963 *Generation of graphs and statistical analysis*

964 All graphs presented in this study were generated using GraphPad PRISM 9. All error bars in this study
965 represent standard deviation. Differences between samples analysed by ANOVA was determined as difference
966 where the p-value was <0.05. For scatterplots, slopes were considered significantly non-zero when the p-value
967 was <0.05.

968 **Data accessibility**

969 This study generated >600 3D Airyscan images of U-ExM parasites at multiple lifecycle stages with
970 multiple combinations of stains. Following any additional imaging that occurs in response peer review, the
971 authors endeavour to make all images freely and publicly available through an online repository. In the
972 interim, the authors will gladly share any of the underlying image datasets through correspondence with the
973 corresponding author.

974 AUTHOR CONTRIBUTIONS

975 **Benjamin Liffner:** Conceptualization, Methodology, Formal analysis, Investigation, Data curation, Writing
976 - Original Draft, Writing - Review & Editing, Visualization.

977 **Ana Karla Cepeda Diaz**: Conceptualization, Methodology, Formal analysis, Investigation, Data curation,
978 Writing - Original Draft, Writing -Review & Editing, Visualization, Funding acquisition.

979 **James Blauwkamp**: Formal analysis, Investigation, Data curation, Writing – Original Draft.

980 **David Anaguano**: Investigation, Writing – Review & Editing.

981 **Sonja Frölich:** Methodology.

982 **Vasant Muralidharan**: Resources, Writing – Review & Editing.

983 **Danny W. Wilson**: Writing -Review & Editing.

984 **Jeffrey Dvorin**: Conceptualization, Resources, Writing –Review & Editing, Supervision, Project
985 Administration, Funding Acquisition.

986 **Sabrina Absalon:** Conceptualization, Methodology, Resources, Writing – Review & Editing, Supervision,
987 Project administration, Funding Acquisition.

988

989

990

ACKNOWLEDGEMENTS

We thank David Roos, Akhil Vaidya, and Rodolpho Ornitz Oliveira Souza for insightful discussions, Vincent Louvel for U-ExM expertise and sharing the protocol for cryopreservation and thawing of gels, and Taco Kooij, and Julie Verhoef for their help with MitoTracker experiments and critical reading of the manuscript. We thank Tobias Spielmann and Isabelle Henshall for generously sharing K13-GFP parasites, and insightful discussion. We thank Julian Rayner, Alan Cowman, Carole Long, BEI Resources (NIAID, NIH), and the European Malaria Reagent Repository for provision of antibodies. This work was supported by NIH R01 AI145941 (JDD) and F31 AI172110 (AKCD).

COMPETING INTERESTS

The authors declare no competing interests.

REFERENCES

1 Kinnunen, M., Kauppila, A., Karmenyan, A. & Myllylä, R. Effect of the size and shape of a red blood cell on elastic light scattering properties at the single-cell level. *Biomed Opt Express* **2**, 1803-1814, doi:10.1364/boe.2.001803 (2011).

2 Wassie, A. T., Zhao, Y. & Boyden, E. S. Expansion microscopy: principles and uses in biological research. *Nature Methods* **16**, 33-41, doi:10.1038/s41592-018-0219-4 (2019).

3 Gambarotto, D. *et al.* Imaging cellular ultrastructures using expansion microscopy (U-ExM). *Nature Methods* **16**, 71-74, doi:10.1038/s41592-018-0238-1 (2019).

4 Rashpa, R. & Brochet, M. Expansion microscopy of *Plasmodium* gametocytes reveals the molecular architecture of a bipartite microtubule organisation centre coordinating mitosis with axoneme assembly. *PLoS Pathog* **18**, e1010223, doi:10.1371/journal.ppat.1010223 (2022).

5 Bertiaux, E. *et al.* Expansion microscopy provides new insights into the cytoskeleton of malaria parasites including the conservation of a conoid. *PLoS Biol* **19**, e3001020, doi:10.1371/journal.pbio.3001020 (2021).

6 Liffner, B. & Absalon, S. Expansion Microscopy Reveals *Plasmodium falciparum* Blood-Stage Parasites Undergo Anaphase with A Chromatin Bridge in the Absence of Mini-Chromosome Maintenance Complex Binding Protein. *Microorganisms* **9**, 2306 (2021).

7 Dave, N., LaFavers, K. & Arrizabalaga, G. The Dually Localized EF-Hand Domain-Containing Protein TgEFP1 Regulates the Lytic Cycle of *Toxoplasma gondii*. *Cells* **11**, doi:10.3390/cells11101709 (2022).

8 Oliveira Souza, R. O., Jacobs, K. N., Back, P. S., Bradley, P. J. & Arrizabalaga, G. IMC10 and LMF1 mediate mitochondrial morphology through mitochondrion-pellicle contact sites in *Toxoplasma gondii*. *J Cell Sci* **135**, doi:10.1242/jcs.260083 (2022).

9 Severo, V. *et al.* Previously Unidentified Histone H1-Like Protein Is Involved in Cell Division and Ribosome Biosynthesis in *Toxoplasma gondii*. *mSphere* **7**, e0040322, doi:10.1128/msphere.00403-22 (2022).

10 Simon, C. S. *et al.* An extended DNA-free intranuclear compartment organizes centrosome microtubules in malaria parasites. *Life Science Alliance* **4**, e202101199, doi:10.26508/lsa.202101199 (2021).

11 Tosetti, N. *et al.* Essential function of the alveolin network in the subpellicular microtubules and conoid assembly in *Toxoplasma gondii*. *eLife* **9**, e56635, doi:10.7554/eLife.56635 (2020).
12 Tomasina, R. *et al.* Separate To Operate: the Centriole-Free Inner Core of the Centrosome Regulates the Assembly of the Intranuclear Spindle in *Toxoplasma gondii*. *mBio* **13**, e01859-01822, doi:doi:10.1128/mbio.01859-22 (2022).
13 Qian, P. *et al.* Apical anchorage and stabilization of subpellicular microtubules by apical polar ring ensures *Plasmodium* ookinete infection in mosquito. *Nature Communications* **13**, 7465, doi:10.1038/s41467-022-35270-w (2022).
14 Nanda, J. S. & Lorsch, J. R. Labeling a protein with fluorophores using NHS ester derivitization. *Methods Enzymol* **536**, 87-94, doi:10.1016/b978-0-12-420070-8.00008-8 (2014).
15 Marks, D. L., Bittman, R. & Pagano, R. E. Use of Bodipy-labeled sphingolipid and cholesterol analogs to examine membrane microdomains in cells. *Histochem Cell Biol* **130**, 819-832, doi:10.1007/s00418-008-0509-5 (2008).
16 Rudlaff, R. M., Kraemer, S., Marshman, J. & Dvorin, J. D. Three-dimensional ultrastructure of *Plasmodium falciparum* throughout cytokinesis. *PLOS Pathogens* **16**, e1008587, doi:10.1371/journal.ppat.1008587 (2020).
17 Grüring, C. *et al.* Development and host cell modifications of *Plasmodium falciparum* blood stages in four dimensions. *Nat Commun* **2**, 165, doi:10.1038/ncomms1169 (2011).
18 Gerald, N., Mahajan, B. & Kumar, S. Mitosis in the human malaria parasite *Plasmodium falciparum*. *Eukaryot Cell* **10**, 474-482, doi:10.1128/ec.00314-10 (2011).
19 Sanchez, A. D. & Feldman, J. L. Microtubule-organizing centers: from the centrosome to non-centrosomal sites. *Curr Opin Cell Biol* **44**, 93-101, doi:10.1016/j.ceb.2016.09.003 (2017).
20 Mahajan, B. *et al.* Centrins, Cell Cycle Regulation Proteins in Human Malaria Parasite *Plasmodium falciparum*. *Journal of Biological Chemistry* **283**, 31871-31883, doi:https://doi.org/10.1074/jbc.M800028200 (2008).
21 Voß, Y., Klaus, S., Ganter, M. & Guizetti, J. Ca^{2+}-inducible phase separation of centrins in proliferating malaria parasites. *bioRxiv*, 2022.2007.2026.501452, doi:10.1101/2022.07.26.501452 (2022).
22 Li, J. *et al.* Repurposing the mitotic machinery to drive cellular elongation and chromatin reorganisation in *Plasmodium falciparum* gametocytes. *Nature Communications* **13**, 5054, doi:10.1038/s41467-022-32579-4 (2022).
23 Rashpa, R., Klages, N., Schvartz, D., Pasquarello, C. & Brochet, M. The Skp1-Cullin1-FBXO1 complex is a pleiotropic regulator required for the formation of gametes and motile forms in *Plasmodium berghei*. *Nature Communications* **14**, 1312, doi:10.1038/s41467-023-36999-8 (2023).
24 Elmendorf, H. G. & Haldar, K. Identification and localization of ERD2 in the malaria parasite *Plasmodium falciparum*: separation from sites of sphingomyelin synthesis and implications for organization of the Golgi. *Embo j* **12**, 4763-4773, doi:10.1002/j.1460-2075.1993.tb06165.x (1993).
25 Kumar, N., Koski, G., Harada, M., Aikawa, M. & Zheng, H. Induction and localization of *Plasmodium falciparum* stress proteins related to the heat shock protein 70 family. *Molecular and Biochemical Parasitology* **48**, 47-58, doi:https://doi.org/10.1016/0166-6851(91)90163-Z (1991).
26 Counihan, N. A., Kalanon, M., Coppel, R. L. & de Koning-Ward, T. F. *Plasmodium* rhoptry proteins: why order is important. *Trends in Parasitology* **29**, 228-236, doi:10.1016/j.pt.2013.03.003 (2013).
27 Ben Chaabene, R., Lentini, G. & Soldati-Favre, D. Biogenesis and discharge of the rhoptries: Key organelles for entry and hijack of host cells by the Apicomplexa. *Molecular Microbiology* **115**, 453-465, doi:https://doi.org/10.1111/mmi.14674 (2021).
28 Machado, M., Klaus, S., Klaschka, D., Guizetti, J. & Ganter, M. *Plasmodium falciparum* CRK4 links early mitotic events to the onset of S-phase during schizogony. *bioRxiv*, 2022.2008.2031.505163, doi:10.1101/2022.08.31.505163 (2022).
29 Liffner, B. & Absalon, S. Hand-in-hand advances in microscopy and *Plasmodium* nuclear biology. *Trends in Parasitology* **38**, 421-423, doi:https://doi.org/10.1016/j.pt.2022.03.007 (2022).
30 Aikawa , M. Ultrastructure of the pellicular complex of *Plasmodium fallax*. *Journal of Cell Biology* **35**, 103-113, doi:10.1083/jcb.35.1.103 (1967).

31 Hanssen, E. *et al.* Electron tomography of *Plasmodium falciparum* merozoites reveals core cellular events that underpin erythrocyte invasion. *Cellular Microbiology* **15**, 1457-1472, doi:https://doi.org/10.1111/cmi.12132 (2013).
32 Morrissette, N. S. & Sibley, L. D. Cytoskeleton of Apicomplexan Parasites. *Microbiology and Molecular Biology Reviews* **66**, 21-38, doi:doi:10.1128/MMBR.66.1.21-38.2002 (2002).
33 Tran, J. Q. *et al.* RNG1 is a late marker of the apical polar ring in *Toxoplasma gondii*. *Cytoskeleton (Hoboken)* **67**, 586-598, doi:10.1002/cm.20469 (2010).
34 Hu, K. Organizational Changes of the Daughter Basal Complex during the Parasite Replication of *Toxoplasma gondii*. *PLOS Pathogens* **4**, e10, doi:10.1371/journal.ppat.0040010 (2008).
35 Francia, M. E. & Striepen, B. Cell division in apicomplexan parasites. *Nature Reviews Microbiology* **12**, 125-136, doi:10.1038/nrmicro3184 (2014).
36 Harding, C. R. & Meissner, M. The inner membrane complex through development of *Toxoplasma gondii* and *Plasmodium*. *Cellular Microbiology* **16**, 632-641, doi:https://doi.org/10.1111/cmi.12285 (2014).
37 Jones, M. L., Kitson, E. L. & Rayner, J. C. *Plasmodium falciparum* erythrocyte invasion: A conserved myosin associated complex. *Molecular and Biochemical Parasitology* **147**, 74-84, doi:https://doi.org/10.1016/j.molbiopara.2006.01.009 (2006).
38 Kono, M. *et al.* Evolution and Architecture of the Inner Membrane Complex in Asexual and Sexual Stages of the Malaria Parasite. *Molecular Biology and Evolution* **29**, 2113-2132, doi:10.1093/molbev/mss081 (2012).
39 Blackman, M. J., Scott-Finnigan, T. J., Shai, S. & Holder, A. A. Antibodies inhibit the protease-mediated processing of a malaria merozoite surface protein. *J Exp Med* **180**, 389-393, doi:10.1084/jem.180.1.389 (1994).
40 Morano, A. A. & Dvorin, J. D. The Ringleaders: Understanding the Apicomplexan Basal Complex Through Comparison to Established Contractile Ring Systems. *Frontiers in Cellular and Infection Microbiology* **11**, doi:10.3389/fcimb.2021.656976 (2021).
41 Rudlaff, R. M., Kraemer, S., Streva, V. A. & Dvorin, J. D. An essential contractile ring protein controls cell division in *Plasmodium falciparum*. *Nature Communications* **10**, 2181, doi:10.1038/s41467-019-10214-z (2019).
42 Anderson-White, B. *et al.* in *International Review of Cell and Molecular Biology* Vol. 298 (ed Kwang W. Jeon) 1-31 (Academic Press, 2012).
43 Roumégous, C. *et al.* Identification of new components of the basal pole of *Toxoplasma gondii* provides novel insights into its molecular organization and functions. *Frontiers in Cellular and Infection Microbiology* **12**, doi:10.3389/fcimb.2022.1010038 (2022).
44 Engelberg, K., Bechtel, T., Michaud, C., Weerapana, E. & Gubbels, M.-J. Proteomic characterization of the *Toxoplasma gondii* cytokinesis machinery portrays an expanded hierarchy of its assembly and function. *Nature Communications* **13**, 4644, doi:10.1038/s41467-022-32151-0 (2022).
45 van Dooren, G. G. *et al.* Development of the endoplasmic reticulum, mitochondrion and apicoplast during the asexual life cycle of *Plasmodium falciparum*. *Molecular Microbiology* **57**, 405-419, doi:https://doi.org/10.1111/j.1365-2958.2005.04699.x (2005).
46 van Dooren, G. G., Stimmler, L. M. & McFadden, G. I. Metabolic maps and functions of the *Plasmodium* mitochondrion. *FEMS Microbiology Reviews* **30**, 596-630, doi:10.1111/j.1574-6976.2006.00027.x (2006).
47 Poot, M. *et al.* Analysis of mitochondrial morphology and function with novel fixable fluorescent stains. *J Histochem Cytochem* **44**, 1363-1372, doi:10.1177/44.12.8985128 (1996).
48 Elmore, S. P., Nishimura, Y., Qian, T., Herman, B. & Lemasters, J. J. Discrimination of depolarized from polarized mitochondria by confocal fluorescence resonance energy transfer. *Arch Biochem Biophys* **422**, 145-152, doi:10.1016/j.abb.2003.12.031 (2004).
49 Wolf, D. M. *et al.* Individual cristae within the same mitochondrion display different membrane potentials and are functionally independent. *The EMBO Journal* **38**, e101056, doi:https://doi.org/10.15252/embj.2018101056 (2019).
50 Evers, F. *et al.* Comparative 3D ultrastructure of *Plasmodium falciparum* gametocytes. *bioRxiv*, 2023.2003.2010.531920, doi:10.1101/2023.03.10.531920 (2023).

51 Evers, F. *et al.* Composition and stage dynamics of mitochondrial complexes in *Plasmodium falciparum*. *Nature Communications* **12**, 3820, doi:10.1038/s41467-021-23919-x (2021).
52 Viswanathan, S. *et al.* High-performance probes for light and electron microscopy. *Nature Methods* **12**, 568-576, doi:10.1038/nmeth.3365 (2015).
53 Esveld, S. L. v. *et al.* A Prioritized and Validated Resource of Mitochondrial Proteins in *Plasmodium* Identifies Unique Biology. *mSphere* **6**, e00614-00621, doi:doi:10.1128/mSphere.00614-21 (2021).
54 Sheiner, L. *et al.* A Systematic Screen to Discover and Analyze Apicoplast Proteins Identifies a Conserved and Essential Protein Import Factor. *PLOS Pathogens* **7**, e1002392, doi:10.1371/journal.ppat.1002392 (2011).
55 Barylyuk, K. *et al.* A Comprehensive Subcellular Atlas of the *Toxoplasma* Proteome via hyperLOPIT Provides Spatial Context for Protein Functions. *Cell Host & Microbe* **28**, 752-766.e759, doi:https://doi.org/10.1016/j.chom.2020.09.011 (2020).
56 Florentin, A., Stephens, D. R., Brooks, C. F., Baptista, R. P. & Muralidharan, V. Plastid biogenesis in malaria parasites requires the interactions and catalytic activity of the Clp proteolytic system. *Proceedings of the National Academy of Sciences* **117**, 13719-13729, doi:doi:10.1073/pnas.1919501117 (2020).
57 Verhoef, J. M. J., Meissner, M. & Kooij, T. W. A. Organelle Dynamics in Apicomplexan Parasites. *mBio* **12**, e0140921, doi:10.1128/mBio.01409-21 (2021).
58 Nishi, M., Hu, K., Murray, J. M. & Roos, D. S. Organellar dynamics during the cell cycle of *Toxoplasma gondii*. *Journal of Cell Science* **121**, 1559-1568, doi:10.1242/jcs.021089 (2008).
59 Francis, S. E., Sullivan, D. J., Jr. & Goldberg, D. E. Hemoglobin metabolism in the malaria parasite *Plasmodium falciparum*. *Annu Rev Microbiol* **51**, 97-123, doi:10.1146/annurev.micro.51.1.97 (1997).
60 Xie, S. C., Ralph, S. A. & Tilley, L. K13, the Cytostome, and Artemisinin Resistance. *Trends in Parasitology* **36**, 533-544, doi:10.1016/j.pt.2020.03.006 (2020).
61 Milani, K. J., Schneider, T. G. & Taraschi, T. F. Defining the morphology and mechanism of the hemoglobin transport pathway in *Plasmodium falciparum*-infected erythrocytes. *Eukaryot Cell* **14**, 415-426, doi:10.1128/ec.00267-14 (2015).
62 Koreny, L. *et al.* Stable and ancient endocytic structures navigate the complex pellicle of apicomplexan parasites. *bioRxiv*, 2022.2006.2002.494549, doi:10.1101/2022.06.02.494549 (2022).
63 Birnbaum, J. *et al.* A genetic system to study *Plasmodium falciparum* protein function. *Nature Methods* **14**, 450-456, doi:10.1038/nmeth.4223 (2017).
64 Yang, T. *et al.* Decreased K13 Abundance Reduces Hemoglobin Catabolism and Proteotoxic Stress, Underpinning Artemisinin Resistance. *Cell Reports* **29**, 2917-2928.e2915, doi:https://doi.org/10.1016/j.celrep.2019.10.095 (2019).
65 Tonkin, C. J. *et al.* Localization of organellar proteins in *Plasmodium falciparum* using a novel set of transfection vectors and a new immunofluorescence fixation method. *Molecular and Biochemical Parasitology* **137**, 13-21, doi:https://doi.org/10.1016/j.molbiopara.2004.05.009 (2004).
66 Aikawa, M. *Plasmodium:* the fine structure of malarial parasites. *Exp Parasitol* **30**, 284-320, doi:10.1016/0014-4894(71)90094-4 (1971).
67 Bannister, L. H., Hopkins, J. M., Fowler, R. E., Krishna, S. & Mitchell, G. H. Ultrastructure of rhoptry development in *Plasmodium falciparum* erythrocytic schizonts. *Parasitology* **121 (Pt 3)**, 273-287, doi:10.1017/s0031182099006320 (2000).
68 Riglar, D. T. *et al.* Super-Resolution Dissection of Coordinated Events during Malaria Parasite Invasion of the Human Erythrocyte. *Cell Host & Microbe* **9**, 9-20, doi:10.1016/j.chom.2010.12.003 (2011).
69 Klaus, S. *et al.* Asynchronous nuclear cycles in multinucleated *Plasmodium falciparum* facilitate rapid proliferation. *Science Advances* **8**, eabj5362, doi:doi:10.1126/sciadv.abj5362 (2022).
70 Topolska, A. E., Lidgett, A., Truman, D., Fujioka, H. & Coppel, R. L. Characterization of a membrane-associated rhoptry protein of *Plasmodium falciparum*. *J Biol Chem* **279**, 4648-4656, doi:10.1074/jbc.M307859200 (2004).
71 Richard, D. *et al.* Interaction between *Plasmodium falciparum* Apical Membrane Antigen 1 and the Rhoptry Neck Protein Complex Defines a Key Step in the Erythrocyte Invasion Process of Malaria Parasites. *Journal of Biological Chemistry* **285**, 14815-14822, doi:https://doi.org/10.1074/jbc.M109.080770 (2010).

72 Ebrahimzadeh, Z. *et al.* A pan-apicomplexan phosphoinositide-binding protein acts in malarial microneme exocytosis. *EMBO reports* **20**, e47102, doi:https://doi.org/10.15252/embr.201847102 (2019).
73 Healer, J., Crawford, S., Ralph, S., McFadden, G. & Cowman, A. F. Independent Translocation of Two Micronemal Proteins in Developing *Plasmodium falciparum* Merozoites. *Infection and Immunity* **70**, 5751-5758, doi:doi:10.1128/IAI.70.10.5751-5758.2002 (2002).
74 Absalon, S. *et al.* Calcium-Dependent Protein Kinase 5 Is Required for Release of Egress-Specific Organelles in *Plasmodium falciparum*. *mBio* **9**, doi:10.1128/mBio.00130-18 (2018).
75 Hale, V. L. *et al.* Parasitophorous vacuole poration precedes its rupture and rapid host erythrocyte cytoskeleton collapse in *Plasmodium falciparum* egress. *Proceedings of the National Academy of Sciences* **114**, 3439-3444, doi:doi:10.1073/pnas.1619441114 (2017).
76 Dubois, D. J. & Soldati-Favre, D. Biogenesis and secretion of micronemes in *Toxoplasma gondii*. *Cellular Microbiology* **21**, e13018, doi:https://doi.org/10.1111/cmi.13018 (2019).
77 de Anda, F. C. *et al.* Centrosome localization determines neuronal polarity. *Nature* **436**, 704-708, doi:10.1038/nature03811 (2005).
78 Cowan, C. R. & Hyman, A. A. Centrosomes direct cell polarity independently of microtubule assembly in *C. elegans* embryos. *Nature* **431**, 92-96, doi:10.1038/nature02825 (2004).
79 Huse, M. Microtubule-organizing center polarity and the immunological synapse: protein kinase C and beyond. *Frontiers in Immunology* **3**, doi:10.3389/fimmu.2012.00235 (2012).
80 Griffith, M. B., Pearce, C. S. & Heaslip, A. T. Dense granule biogenesis, secretion, and function in *Toxoplasma gondii*. *J Eukaryot Microbiol* **69**, e12904, doi:10.1111/jeu.12904 (2022).
81 Sloves, P.-J. *et al.* *Toxoplasma* Sortilin-like Receptor Regulates Protein Transport and Is Essential for Apical Secretory Organelle Biogenesis and Host Infection. *Cell Host & Microbe* **11**, 515-527, doi:10.1016/j.chom.2012.03.006 (2012).
82 Kudryashev, M. *et al.* Structural basis for chirality and directional motility of *Plasmodium* sporozoites. *Cell Microbiol* **14**, 1757-1768, doi:10.1111/j.1462-5822.2012.01836.x (2012).
83 Louvel, V. *et al.* Nanoscopy of organelles and tissues with iterative ultrastructure expansion microscopy (iU-ExM). *bioRxiv*, 2022.2011.2014.516383, doi:10.1101/2022.11.14.516383 (2022).
84 Coronado, L. M., Nadovich, C. T. & Spadafora, C. Malarial hemozoin: from target to tool. *Biochim Biophys Acta* **1840**, 2032-2041, doi:10.1016/j.bbagen.2014.02.009 (2014).
85 Geoghegan, N. D. *et al.* 4D analysis of malaria parasite invasion offers insights into erythrocyte membrane remodeling and parasitophorous vacuole formation. *Nature Communications* **12**, 3620, doi:10.1038/s41467-021-23626-7 (2021).
86 Weiss, G. E. *et al.* Revealing the Sequence and Resulting Cellular Morphology of Receptor-Ligand Interactions during *Plasmodium falciparum* Invasion of Erythrocytes. *PLOS Pathogens* **11**, e1004670, doi:10.1371/journal.ppat.1004670 (2015).
87 Liffner, B. *et al.* Cell biological analysis reveals an essential role for *Pfcerli2* in erythrocyte invasion by malaria parasites. *Communications Biology* **5**, 121, doi:10.1038/s42003-022-03020-9 (2022).
88 Ferreira, J. L. *et al.* The Dynamic Roles of the Inner Membrane Complex in the Multiple Stages of the Malaria Parasite. *Frontiers in Cellular and Infection Microbiology* **10**, doi:10.3389/fcimb.2020.611801 (2021).
89 Trager, W. & Jensen, J. B. Human malaria parasites in continuous culture. *Science* **193**, 673-675, doi:10.1126/science.781840 (1976).
90 Lambros, C. & Vanderberg, J. P. Synchronization of *Plasmodium falciparum* erythrocytic stages in culture. *J Parasitol* **65**, 418-420 (1979).
91 Salmon, B. L., Oksman, A. & Goldberg, D. E. Malaria parasite exit from the host erythrocyte: a two-step process requiring extraerythrocytic proteolysis. *Proceedings of the National Academy of Sciences* **98**, 271-276 (2001).
92 Taylor, H. M. *et al.* The Malaria Parasite Cyclic GMP-Dependent Protein Kinase Plays a Central Role in Blood-Stage Schizogony. *Eukaryotic Cell* **9**, 37-45, doi:doi:10.1128/EC.00186-09 (2010).